THE ELECTRONIC AND THERMODYNAMIC PROPERTIES

OF Ca DOPED LaFeO$_3$ – A FIRST PRINCIPLES STUDY

USING DENSITY FUNCTIONAL THEORY

by

Davis George Daniel

A thesis

submitted in partial fulfillment

of the requirements for the degree of

Master of Science in Materials Science and Engineering

Boise State University

August 2014

BOISE STATE UNIVERSITY GRADUATE COLLEGE

DEFENSE COMMITTEE AND FINAL READING APPROVALS

of the thesis submitted by

Davis George Daniel

Thesis Title: The Electronic and Thermodynamic Properties of Ca doped $LaFeO_3$ –
A First Principles Study Using Density Functional Theory

Date of Final Oral Examination: 18 April 2014

The following individuals read and discussed the thesis submitted by student Davis George Daniel, and they evaluated his presentation and response to questions during the final oral examination. They found that the student passed the final oral examination.

Darryl P. Butt, Ph.D.   Co-Chair, Supervisory Committee

Pushpa Raghani, Ph.D.   Co-Chair, Supervisory Committee

Lan Li, Ph.D.   Member, Supervisory Committee

The final reading approval of the thesis was granted by Darryl P. Butt, Ph.D., Co-Chair of the Supervisory Committee and Pushpa Raghani, Ph.D., Co-Chair of the Supervisory Committee. The thesis was approved for the Graduate College by John R. Pelton, Ph.D., Dean of the Graduate College.

ACKNOWLEDGEMENTS

ABSTRACT

Density functional theory (DFT) was used to evaluate the electronic and thermodynamic properties of Ca-doped $LaFeO_3$ ($La_{1-x}Ca_xFeO_{3-y}$). $La_{1-x}Ca_xFeO_{3-y}$ exhibits ionic (O^{2-} anions) and electronic conductivity at high temperatures and has potential applications in gas separation, syngas production, and solid oxide fuel cell cathodes. DFT is a computational technique based on the First Principles of physics, derived from the theory of quantum mechanics. DFT approximates the ground state energy of a system and can subsequently determine many bulk properties such as lattice constants, magnetic states, band gap, density of states (DOS), and defect formation energy (DFE).

The calculated ground state structure for $LaFeO_3$ was assumed to be orthorhombic and the optimized magnetic state was the G-type antiferromagnetic. The Hubbard U (DFT+U) method successfully corrected the underestimated band gap and magnetic moment of Fe for the orthorhombic $LaFeO_3$ system. The electronic structures (DOS) indicated the substitution of Ca atoms introduced holes; while an oxygen vacancy introduced extra electrons and the combination of these defects annihilate the defect states. The calculated DFE indicated the addition of a Ca atom is energetically favorable, but the formation of an oxygen vacancy was energetically very unfavorable. The combination of the two defects lowered the DFE considerably, indicating that the ionic conductivity in $LaFeO_3$ can be substantially increased with the introduction of Ca atoms.

TABLE OF CONTENTS

LIST OF FIGURES

LIST OF ABBREVIATIONS

ABO$_3$ Perovskite oxides

AFM   Antiferromagnetic

BSU   Boise State University

CB   Conduction band

CBM   Conduction band maximum

DFE   Defect formation energy

DFT   Density Functional Theory

DOS   Density of States

E$_{cut}$ Kinetic energy cutoff

E$_F$ Fermi energy

FCC   Face-centered cubic

FM   Ferromagnetic

GGA   General gradient approximation

HS   High spin

LCF   Lanthanum calcium ferrite (La$_{1-x}$Ca$_x$FeO$_{3-y}$)

LDA   Local density approximation

LF	Lanthanum ferrite (LaFeO$_3$)
NM	Non-magnetic
PBE	Perdew–Burke–Ernzerhof
PDOS	Partial Density of States
PES	Photoemission spectroscopy
QE	Quantum Espresso – Plane wave code based on DFT
RBM	Rigid-Band Model
SCF	Self-consistent field
SE	Schrödinger equation
VB	Valance band
VBM	Valence band maximum
XAS	X-Ray adsorption spectroscopy

1. INTRODUCTION

1.1 Motivation for Research

Perovskite oxides in the form of ABO_3 (A: alkaline-earth metal or La, B: $3d$ transition metal, O: oxygen) are robust and flexible chemical platforms, which exhibit novel properties. In the ABO_3 system, the A site is occupied for example by Ca, Ba, Sr, or La atoms, while the B site is occupied for example by Mn, Co, Fe, or Cr atoms, resulting in perovskites with desired properties and performance. The variety of A and B atoms can tailor the structural, magnetic, electronic, and thermodynamic properties of the perovskites, depending on the size and valence electrons of the A and B atoms.

The ABO_3 perovskites of interest in this thesis are perfect $LaFeO_3$ (LF) and $LaFeO_3$ with defects, such as Ca substitution at La sites and oxygen vacancies. The three defect configurations are $LaFeO_{3-y}$, $La_{1-x}Ca_xFeO_3$, and $La_{1-x}Ca_xFeO_{3-y}$ (LCF). Due to the defects, LCF exhibits ionic (O^{2-} anions) and electronic conductivity at high temperatures.[1, 2] These unique properties make LCF a promising candidate for high temperature applications, such as syngas production.[3, 4]

Previous experimental work conducted at Boise State University (BSU) has examined the bulk properties of various perovskite-oxide systems including the LCF system.[5] This thesis utilizes Density Functional Theory (DFT) to evaluate the bulk properties of LF and the different defects systems such as Ca doping and oxygen vacancies. DFT is based on First Principles of physics, derived from the theory of

quantum mechanics.[6] The theory overcomes the many-body problem in quantum mechanics by approximating the solution of the Schrödinger equation, to determine the ground-state energy, and thereby all the properties of the system. Today, the accuracy and reliability of DFT calculations and its subsequent successful theoretical predictions have made it a multidisciplinary tool, in fields including physics, chemistry, geology and materials science.[6] The theoretical predictions obtained from DFT can guide experiments and reduce production cost.

1.2 Objectives

The initial objective is to determine the ground state crystal and magnetic structure of LF. The two crystal structures of interest are cubic and orthorhombic LF and the four magnetic structures of interest are the A-type, C-type, G-type antiferromagnetic (AFM), and ferromagnetic (FM) states. Once the ground state structure of LF is obtained, its electronic structure will be studied in greater detail, by analyzing the density of states (DOS) and partial density of states (PDOS). To accurately predict the magnetic and electronic properties of LF, the Hubbard U model is applied to correct the inherent errors presented within the generic DFT techniques.

The final objective is to obtain the electronic and thermodynamic properties of three defects systems: $La_{1-x}Ca_xFeO_3$, $LaFeO_{3-y}$, and $La_{1-x}Ca_xFeO_{3-y}$. The defect electronic structures (DOS and PDOS) are evaluated, using the rigid-band model (RBM) and the thermodynamic properties are evaluated, using the formalism, known as defect formation energy (DFE).

2. BACKGROUNDS AND PRIOR LITERATURE

2.1 Experimental Observations

2.1.1 The Crystal Structures of $LaFeO_3$
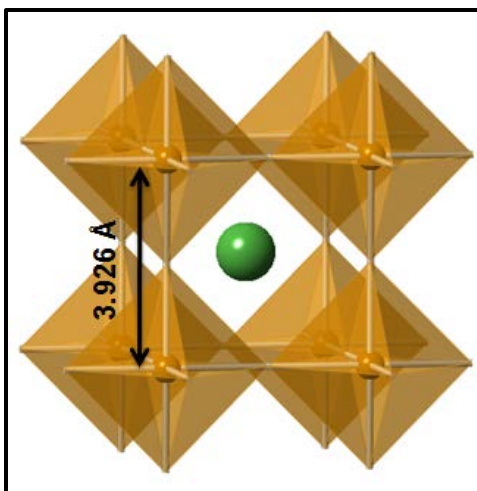
Figure 1. **The ideal cubic structure of $LaFeO_3$, the La atom is at the center (green sphere) and the FeO_6 octahedral form at the corners. The experimental cubic lattice constant[7] is included. The color image is available online.**

Figure 1 shows the ideal cubic LF structure (space group Pm-3m) with an experimental lattice constant of 3.926 Å and the unique atomic positions are: La 1b (0.5, 0.5, 0.5), Fe 1a (0, 0, 0), and O 3d (0, 0, 0.5).[7] The La atom occupies the center of the cube, while the Fe atoms at the corners bond with the adjacent oxygen atoms to form the FeO_6 octahedra. LF does not exist in the pristine cubic regime, and at ambient conditions has the orthorhombic structure.[8]
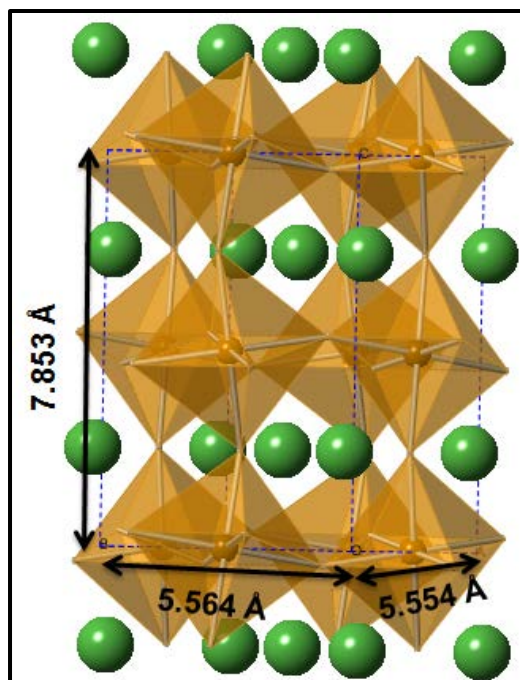
Figure 2. **The orthorhombic LaFeO₃ structure, green spheres are La atoms and each Fe is surrounded by six O atoms to form the FeO₆ octahedral. The experimental lattice constants gathered at BSU are included. The color image is available online.**

The ground state energy configuration requires octahedral titling and distortion in the LF structure, which reduces the symmetry from cubic to orthorhombic. Figure 2 shows LF as the orthorhombic $GdFeO_3$ type perovskite, with the space group Pnma, where the lattice constants a ≠ b ≠ c and the angles $\alpha = \beta = \gamma = 90^o$.[5] The Pnma structure can be approximated using the cubic lattice parameter a_{cubic}, where the Pnma lattice constants are $a = b = (2a_{cubic})^{1/2}$ and $c = 2a_{cubic}$. In the Pnma structure, the La, Fe and O atoms have 12, 6, and 6-fold coordination, respectively.

Table 1. **Comparing the different experimental lattice constants of orthorhombic LaFeO$_3$ and the numbers in parentheses represent the standard deviation or uncertainty of the last digit.**

Lattice Constants (Å)	Beausoleil et al.[5]	Taguchi et al.[9]	Dann et al.[10]
a	5.5602($\pm$ 0.0002)	5.5509(5)	5.5553(8)
b	5.5679($\pm$ 0.0002)	5.5595(4)	5.5663(8)
c	7.8550($\pm$ 0.0003)	7.8498(7)	7.8545(13)

Table 2. **The experimental atomic positions of orthorhombic LaFeO$_3$ and the numbers in parentheses represent the uncertainty of the last digit.[10]**

Atomic site	Position	x	y	z
La	4(c)	0.9923(4)	0.0292(1)	0.25
Fe	4(b)	0	0	0
O	4(c)	0.0748(4)	0.4855(3)	0.25
O	8(d)	0.7191(2)	0.2817(1)	0.0394(1)

Tables 1 and 2 indicate the different experimental lattice parameters and atomic positions of orthorhombic LF. In this study, the atomic position of Fe (Table 2) was corrected from (0, 0, 0) to (0, 0.5, 0) to obtain the correct orthorhombic structure.

2.1.2 The Electronic and Magnetic Properties of $LaFeO_3$
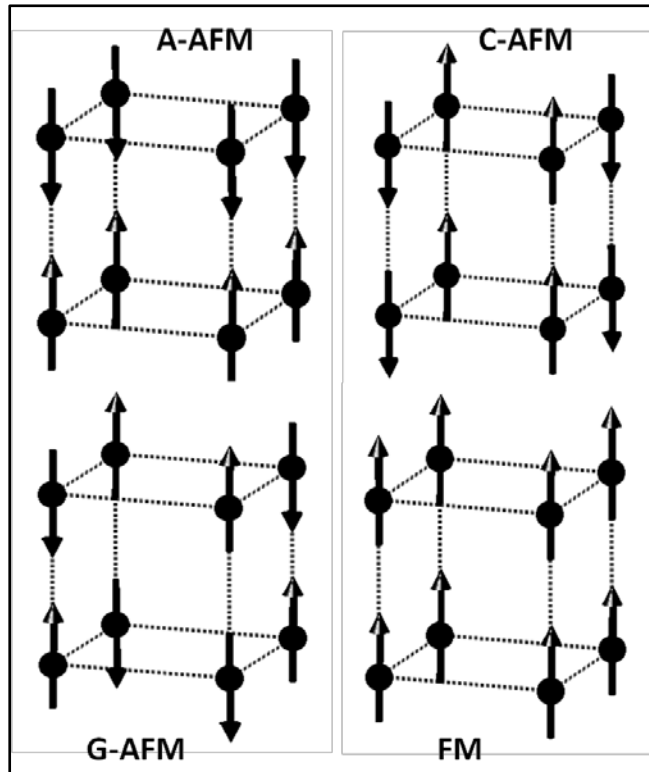
Figure 3. **The different magnetic configurations: A-type, C-type, G-type AFM, and FM are shown, using the up and down magnetic spins of the Fe atoms (spheres). Picture modified from Shein *et al.*[11]**

Figure 3 shows the different magnetic configurations such as A-AFM, C-AFM, G-AFM, and FM, in a cubic perspective, using spin up and down Fe atoms.[11] Previous neutron diffraction experiments investigating the magnetic properties have shown that LF has the G-AFM configuration.[7] The Néel temperature is the temperature at which an antiferromagnetic or ferromagnetic state changes to paramagnetic. For orthorhombic LF, the Néel temperature is 750 K and the observed magnetic moment for Fe, gathered from low temperature coherent magnetic reflections is 4.6 ± 0.2 μ_B.[7] Previous experimental work indicates that LF is an insulator.[12] Arima *et al.*[12] used optical spectroscopy to obtain the band structure of LF, and found an optical band gap of 2.1 eV. The observed optical band gap was between the valence band (VB), which is dominated by occupied O $2p$

orbitals, and the conduction band (CB), which is dominated by unoccupied Fe $3d$ orbitals.[12] According to Wadati *et al.*[13], the photoemission spectroscopy (PES) and x-ray adsorption spectroscopy (XAS) spectra experiments provide great insight on the presence and nature of orbitals near the E_F (Fermi energy) for LF. In orthorhombic LF, the Fe valence electrons are in the high spin (HS) configuration.[13] In the valence region, the key features below the E_F can be broken into three configurations A, B, and C. The A and B configurations are dominated by the occupied e_g and t_{2g} bands of the Fe $3d$ orbitals, respectively.[13] The C configuration is dominated by states that indicate the covalent bonding between the Fe $3d$ and O $2p$ orbitals.[13] In the conduction region, the key features above the E_F can be broken into two configurations, D and E, which are dominated by the unoccupied e_g and t_{2g} bands of the Fe $3d$ orbitals, respectively.[13] The split between the e_g and t_{2g} bands can be described using crystal-field theory.[13] In the conduction region above the unoccupied Fe $3d$ orbitals are the unoccupied La $5d$ orbitals.[13]

2.1.3 Bulk Properties of $La_{1-x}Ca_xFeO_{3-y}$

Under ambient conditions, the LCF structure still maintains the orthorhombic configuration, with the space group Pnma.[5] The charge imbalance due to the introduction of divalent Ca^{2+} atoms at trivalent La^{3+} sites is compensated by the formation of oxygen vacancies.[5] The formation of these point defects (Ca^{2+} cations and O^{2-} anions) leads to novel ionic and electronic conductivities at high temperatures.[1, 2, 3, 4, 14]

2.1.4 Energetics of Bulk Oxides

To evaluate thermodynamic properties of defects with DFT requires the use external potentials. The external potentials of interest are μ_{La}, μ_{Fe}, and μ_{Ca}, which can be

determined from the total energies of bulk oxides, such as La_2O_3, Fe_2O_3, and CaO, respectively.

Lanthanum oxide (La_2O_3) is a rare-earth sesquioxide; it has a hexagonal structure and the space group is $P6_3/mmm$.[15] The experimental lattice constants of La_2O_3 are, a = 3.940 Å and c = 6.130 Å, respectively.[16] The unit cell of La_2O_3 has five unique atomic sites, two La atoms occupy the 2d sites at ± (1/3, 2/3, u), two O atoms occupy the 2d sites at ± (1/3, 2/3, v), and the last O atom occupy the 1a site at (0, 0, 0).[17] Neutron diffraction studies have confirmed these atomic positions and indicated that the two internal degrees of freedom parameters, u and v, are 0.245 and 0.645, respectively.[16]

Iron oxide (Fe_2O_3), commonly known as hematite, has a rhombohedral structure and the space group is R-3c.[18] At ambient conditions, Fe_2O_3 has an antiferromagnetic structure, where the Fe atoms arrange along the [111] axis, in the primitive rhombohedral structure.[19] Blanchard et $al.$[20] derived the experimental rhombohedral lattice parameter a = 5.427 Å and the angle α = 55.280° from a previous experimental work[21], which used a hexagonal structure.

Table 3. **The experimental atomic positions of Fe and O atoms in the primitive rhombohedral Fe_2O_3 structure. The two degrees of freedom, r and s, are 0.10534(6) and 0.3056(9). Numbers in parenthesis are the uncertainty associated with the last digit.**[18, 22]

Atomic site	x	y	z
1. Fe	r	r	r
2. Fe	0.5 − r	0.5 − r	0.5 − r
3. Fe	0.5 + r	0.5 + r	0.5 + r
4. Fe	1 − r	1 − r	1 − r
1. O	s	1 − s	0
2. O	1 − s	0	s
3. O	0	s	1 − s
4. O	0.5 − s	0.5 + s	0.5
5. O	0.5 + s	0.5	0.5 − s
6. O	0.5	1 − s	0.5 + s

As shown in Table 3, the primitive rhombohedral unit cell of Fe_2O_3 has 10 unique atomic sites. According to the Wyckoff notation, in the Fe_2O_3 unit cell, the four Fe atoms occupy the 4c sites and the six O atoms occupy the 6e sites, respectively.[17] As shown in Table 3, the two degrees of freedom, r and s, are 0.10534(6) and 0.3056(9), numbers in parenthesis is the uncertainty associated with the last digit.[18, 22]

Calcium oxide (CaO) is a wide-gap insulator; it has a rock-salt structure, with the space group Fm3m.[23] The experimental lattice constant of CaO is a = 4.81 Å.[24] The face-centered cubic (FCC) CaO unit cell has two unique atomic positions, each Ca and O atom occupy the sites (0, 0, 0) and (0.5, 0.5, 0.5), respectively.[25]

2.2 First-Principles Methods

The key ideas and equations in this section were gathered from Lee.[26] The key breakthrough in quantum mechanics was in 1926 when Erwin Schrödinger found an accurate mathematical description for the wave nature of matter.[26] The Schrödinger equation (SE) is described as:

$$\hat{H}\psi = E\psi \tag{1}$$

where $\hat{H}$ is the Hamiltonian operator, ψ is the wave function, and E is the energy. The wave function ψ describes the quantum mechanical properties of the material, and the Hamiltonian operator $\hat{H}$ is applied on ψ, to obtain the energy (E) of the system. Rewriting the SE for a real system, which includes all the dimensions, is given as:

$$\hat{H}\psi(r_i, r_I, t) = E\psi(r_i, r_I, t) \tag{2}$$

where r_i, r_I are the coordinates of the electron and nuclei, and t is time.[26] To illustrate the many-body problem, take an oxygen atom that has eight electrons, and so the total electronic coordinates, $r_i = 3n = 3 \times 8 = 24$ dimensions. Currently, no methodology exists to exactly solve problems with more than three dimensions.

Rather than shelving this seemingly not solvable SE, certain steps are taken to reduce the dimensions of the problem, to approximate the ground-state energy. The first step is to make it a time-independent problem, which reduces the SE to:

$$\hat{H}\psi(r_i, r_I) = E\psi(r_i, r_I) \tag{3}$$

A proton is 1836 times heavier than an electron; this difference in mass makes electrons interact/react instantaneously to external forces, whereas the nuclei is generally unaffected.[26] Therefore, the Born-Oppenhimer approximation separates the nuclear and electronic contributions of the total energy.

$$E_{atom} = E_{nucleus} + E_{electron} \tag{4}$$

Now the energy terms are simplified, where the nucleus is a static contributor and its dimensions are cancelled. The Born-Oppenhimer approximation reduces the SE to:

$$\hat{H}\psi(r_i) = E\psi(r_i) \tag{5}$$

Even with this simplified version of the SE, further approximations need to be included to compute the approximate ground state energy. For this, a closer look at the SE's individual components, such as the $\hat{H}$, ψ, and E, need to be further analyzed. The Hamiltonian $\hat{H}$ is the energy operator, which includes all the unique energy contributors of the system, both kinetic and potential energy terms. The electrons and nuclei have kinetic energies in the form E_i^{kin} and E_I^{kin}, respectively.[26] The potential energy terms are due to the Columbic interactions between the nucleus-electron (U_{Ii}), electron-electron (U_{ij}), and nucleus-nucleus (U_{IJ}).[26] Combining all the kinetic and potential energy terms, the expanded Hamiltonian $\hat{H}$ is described as:

$$\hat{H} = E_i^{kin} + E_I^{kin} + U_{Ii} + U_{ij} + U_{IJ} \tag{6}$$

Applying the Born-Oppenheimer approximation, the Hamiltonian reduces to:

$$\hat{H} = E_i^{kin} + U_{Ii} + U_{ij} \tag{7}$$

The first term E_i^{kin} is the kinetic energies of the n electrons in the system, described as:

$$E_i^{kin} = -\frac{\hbar^2}{2m}\sum_i^n \nabla_i^2 = -\frac{1}{2}\sum_i^n \nabla_i^2 \tag{8}$$

where ∇^2 is the Laplacian operator, defined as:

$$\nabla^2 = \frac{\partial^2}{\partial x^2} + \frac{\partial^2}{\partial y^2} + \frac{\partial^2}{\partial z^2} \tag{9}$$

The second Hamiltonian term U_{Ii} is the attractive potential energy between the electrons and nuclei, described as:

$$U_{Ii} = -\sum_I^N \sum_i^n \frac{Z_I}{|r_{Ii}|} \tag{10}$$

where N and n are the total number of nuclei and electrons, Z_I is the charge of the nuclei.[26] In equation (10), the sum $\sum\sum$ includes all the interactions between all the electrons and nuclei. The nuclei are still considered a frozen and static entity, which imposes an external potential, but does not interact with the electrons.

The third Hamiltonian term (U_{ij}) is a repulsive potential interaction between the n electrons, where a correction factor ½ to avoid double-counting.

$$U_{ij} = \frac{1}{2}\sum_{i\neq j}^n \frac{1}{|r_{ij}|} \tag{11}$$

Summing all the energy kinetic and potential terms, the Hamiltonian Ĥ is described as:

$$\hat{H} = -\frac{1}{2}\sum_i^n \nabla_i^2 - \sum_I^N \sum_i^n \frac{Z_I}{|r_{Ii}|} + \frac{1}{2}\sum_{i\neq j}^n \frac{1}{|r_{ij}|} \tag{12}$$

This simplified Hamiltonian has all the energy terms, and the use of the electron density instead of ψ makes it finally possible to approximate the energy E of the system. This numerical approximation to obtain the energy of a system is known as DFT.

2.3 Density Functional Theory

2.3.1 Introduction

The key ideas and equations in this section were gathered from Lee.[26] Due to the many-body problem, the SE could not be solved exactly for real systems and an accurate approximation of the ground state energy could only be obtained by computational techniques. The first computational effort to approximate the SE was the Hartree method. Due to oversimplifications within the Hartree method to approximate the ground state energy, it was severely limited to accurately study only very simple systems. A proposed improvement was the Hartree-Fock method, which was more accurate, but only limited to systems with tens of atoms.[26]

2.3.2 Foundations of DFT

The Hartree method had established three keys foundations, used by all First Principle computational methodologies, including DFT. The three key topics are:[26]

1. Replacing ψ: The Hartree method replaced the wavefunction ψ, with one-electron wave functions (electron density), to describe the electrons. The Hartree method avoided the many-body problem by having non-interacting electrons in a mean field potential.

2. Variational principle: Except for degenerate systems, every material has a unique ground state energy that cannot be lowered. The variational principle claims that when the most minimum energy is calculated within a given error, it is the ground state energy of the system.

3. Self-consistent method: A particular routine is adopted to solve the wave equations to obtain the ground state energy:

   a) Obtain an appropriate set of wave functions.

   b) Calculate the electron density and energy terms of the Hamiltonian.

   c) Insert previously obtained values into the wave equation and solve for the new wave functions and energy.

   d) Continue steps a – c, until the calculated wave functions are equal to the initial wave functions, within a predetermined energy accuracy margin. The energy obtained from the final wavefunction is the ground state energy of the system.

2.3.3 Hohenberg-Kohn Theorems

Both the Hartree and Hartree-Fock methods use the electron density, variational principle, and the self-consistent approach to approximate the solutions of the SE and calculate the ground state energy. But, in 1964, Hohenberg and Kohn proposed two theorems that formally legitimized the connection between the "electron density, external potential, Hamiltonian and wave functions."[26] The two theorems are:[26]

1. Electron density: The first theorem states that there is a direct relationship between the external potential (interaction of the nuclei and electrons) and the electron density. The electron density can be used to calculate the external potential and vice-versa. Therefore, at the ground state energy, there is only a unique electron density and a corresponding external potential.

2. Variational principle: The second theorem utilizes the variational principle to determine the ground state energy by optimizing the electron density of the system. The electron density that produces the lowest minimum energy is the ground state electron density.

2.3.4 The Kohn-Sham Methodology (DFT)

In 1965, Kohn and Sham proposed a computational methodology to apply the two newly found Hohenberg-Kohn theorems to compute ground state energetics. Just like in the Hartree formalism, the Kohn-Sham approach (DFT) used the fictional one-electron representation for the wave functions, but divided the Hamiltonian energy terms into interacting and non-interacting terms for a given external potential.[26] Combining all the energy terms to compute the total energy gives:

$$E = E_{kin}^{non} + E_{ext} + E_H + E_{XC} = F[\rho(r)] + E_{XC} \tag{13}$$

The term $F[\rho(r)]$ is the combination of all the non-interacting energy terms, which can be described by the electron density and can be computed exactly. The term E_{XC} is the combination of two interacting energy terms, which includes the kinetic and correlation energy (electron-electron interactions) contributions. The term E_{XC} cannot be solved exactly due to the many-body problem, but can be approximated. This approximation improves the accuracy of the ground state energy and distinguishes DFT when compared to the Hartree or Hartree-Fock methods.[26]

2.3.5 Solving the Kohn-Sham Equations

Once the different energy contributions are written in terms of either the electron density or as Kohn-Sham orbitals, a self-consistent routine is used to solve the final Kohn

Sham equation to determine the ground state energy.[26] The final Kohn-Sham equation is described as:

$$\hat{H}_{KS}\phi_i(r) = \varepsilon_i\phi_i(r) \qquad (14)$$

The term $\hat{H}_{KS}$ is the Kohn-Sham Hamiltonian and $\phi_i(r)$ are Kohn-Sham orbitals in terms of single-electron orbitals. Generally, a self-consistent routine to find the ground state energy in DFT is the following procedure:[26]

1. Choose the initial electron density and external potential.

2. Calculate the energy terms in the $\hat{H}_{KS}$.

3. Insert the energy terms and solve the Kohn-Sham equation to find the new Kohn-Sham orbitals.

4. Determine new electron density.

5. Repeat steps 1 – 4 until the ground state energy is achieved within a preset error margin.

Generally, the self-consistent procedure fixes the forces and positions of the atoms, more rigorous procedures could find the ground state energy by optimizing the atomic positions, forces, and lattice parameters simultaneously.

2.3.6 Important Input Parameters

There are few input parameters that are optimized to find a compromise between expediting the computational procedure to find the ground state energy, but with an appropriate accuracy.[26]

The wave functions of a system depend on the electronic configurations of the constituent atom(s). The pseudopotential simplifies these wave functions to expedite the computational procedure. Generally valence electrons participate in chemical reactions, bond formation, electronic structure, and thermodynamic properties of materials. Therefore, the pseudopotential approach freezes the nucleus and core electrons into an approximated potential. The wave functions of the valence electrons are only considered, and using the pseudopotential approach further simplifies these wave functions.[26]

K-Points are unique points used to solve the Kohn-Sham equations within the irreducible Brillouin zone. Systems with high symmetry utilize less K-Points, thereby expediting the computation procedure; likewise systems with low symmetry require more K-Points, which increase the computational time. The K-Points is a system-dependent term, and is optimized to not only expedite the computational procedure, but to provide acceptable accurate results too.[26]

Kinetic energy cutoff (E_{cut}) is a system-dependent term, which is included to restrict the wave function expansion to a finite value. The E_{cut} term is optimized to not only expedite the computational procedure, but to provide acceptable accurate results too.[26]

Generally, a supercell approach is applied when a "nonperiodic entity" such as a defect is included in to the system.[26] The size of the supercell is optimized to avoid any unphysical interaction between the defect and corresponding images.[26]

2.4 Density Functional Theory Literature

2.4.1 Cubic LaFeO$_3$

The cubic LF system has been extensively studied using DFT to determine its properties for high-temperature applications.[8, 27, 28] Investigators have used either pristine cubic LF structure with the space group Pm-3m,[8, 11, 28] or a pseudo-cubic structure where the atoms have a GdFeO$_3$-type distortion.[27] The experimental magnetic state of cubic LF is not known; therefore, previous calculations have no consensus on this topic, but display a variety of ground state magnetic configurations from G-AFM, FM, and NM (non-magnetic).[8, 11, 28] Generally, the calculated lattice constant (a_o = 3.821 Å[27]) for cubic LF is underestimated to the experimentally derived value of a_o = 3.926 Å.[7] The addition of the Hubbard U term increases the lattice constant considerably to a_o = 3.943 Å.[27]

The cubic LF structure is considered to be metallic in nature due to the delocalization of the Fe electrons within the lattice. Lee *et al.*[27] utilized a pseudo-cubic configuration and their DOS indicated cubic LF to be metallic. The PDOS indicated that there were unoccupied Fe orbitals at the E_F, which made the system metallic.[27]

2.4.2 Orthorhombic LaFeO$_3$

The orthorhombic LF structure has been extensively studied using the DFT methodology. Various investigators concluded that the calculated ground state is the G-AFM orthorhombic structure with the space group Pnma, which is consistent with experimental findings.[5, 29, 30]

Table 4. **Comparing the calculated and experimentally observed lattice constants of orthorhombic LaFeO$_3$.**

	Method	a (Å)	b (Å)	c (Å)
Kizaki & Kusakabe.[29]	DFT	5.513	5.627	7.857
Ritzmann et al.[30]	DFT	5.556	5.653	7.885
Beausoleil et al.[5]	Experimental	5.5602	5.5679	7.8550

As shown in Table 4, the previously calculated lattice constants of orthorhombic LF is in good agreement with observed experimental values.[5, 29, 30] Various DFT computational evaluations have produced an accurate electronic description for the orthorhombic LF structure when compared with experimental findings.[7, 12, 29, 30]

Table 5. **Comparing the calculated and experimentally observed band gap and magnetic moment of Fe for orthorhombic LaFeO$_3$.**

	Method	E$_g$ (eV)	μ$_B$ / Fe atom
Kizaki & Kusakabe.[29]	DFT	0.89	4.1
Ritzmann et al.[30]	DFT	0.75	3.7
Koehler & Wollan.[7] Arima et al.[12]	Experimental	2.1	4.6±0.2

As shown in Table 5, the calculated band gaps predict orthorhombic LF to be an HS insulator, in agreement with experimental observations too. The apparent underestimation of the calculated band gaps is a common error found in generic DFT calculations.[31] The band gap can be improved with artificial correction methods, particularly the Hubbard U model. The underestimation of the magnetic moment of the

Fe atom is not as severe, and agrees well with the experimental value. Also, the magnetic moment can be improved too using the Hubbard U model.

DFT has successfully confirmed that the orthorhombic LF is a ligand-to-metal charge transfer insulator.[29] The PDOS shows that the valence band maximum (VBM) is dominated by both Fe *3d* and O *2p* states, indicating a high degree of hybridization of Fe-O orbitals. The conduction band maximum (CBM) band is dominated by the unoccupied Fe *3d* orbitals.[29, 30]

2.4.3 Hubbard U Model

Generally, generic DFT calculations underestimate the band gaps for semiconductors and insulators. This error is due to the incorrect description of the electronic structures of highly correlated systems. This correlation is the consequence of the hybridization between the localized *d* and *f* orbitals with other *s* or *p* orbitals.[32] These inherent shortcomings are caused by the inability of the exchange and correlation energy approximations, within the general gradient approximation (GGA) functional, to meet the requirements to properly describe these highly correlated orbitals.[32] In these highly correlated systems, it is common to find partially or half-filled orbitals and the self-interaction error of these orbitals are not completely removed, which is a major contributor to the band gap problem.[26] Therefore, when band positions are represented by occupation numbers between 0 and 1 (non-integer values), it pushes the valence band up and conduction band down, thereby narrowing the band gap.[26]

There is a technique to overcome this problem, the implementation of the Hubbard U model, better known as the DFT+U methodology, to correct the self-interaction error.[32, 33] Generally, the incorrect total energy DFT curve includes energy

contributions from integer and non-integer value orbitals and this curve is parabolic in nature.[32] With the implementation of DFT+U, the energy curve becomes piecewise and linear in nature, including only the contributions from integer value orbitals.[32] Therefore, the application of the Hubbard U correction term provides an opportunity to obtain the real and physical total energy description of highly correlated systems. Both authors proposed a linear-response approach to find the Hubbard U value; this approach is a self-consistent technique, which does not utilize any experimental results.[32, 33]

Generally, DFT evaluations have regularly underestimated the band gap and magnetic moment of Fe for the orthorhombic LF structure. Generally, the addition of the Hubbard U term has corrected the band gap problem, by increasing the previously underestimated band gap.[34]

Table 6. **Comparing the calculated and experimentally observed band gap and magnetic moment of Fe for orthorhombic LaFeO$_3$.**

	Method	E$_g$ (eV)	μ_B / Fe atom
Yang *et al.*[34]	DFT+U	2.1	4.1
Ritzmann *et al.*[30]	DFT+U	2.53	4.1
Koehler & Wollan.[7] Arima *et al.*[12]	Experimental	2.1	4.6±0.2

Table 6 indicates the use of DFT+U improves the calculated band gap and magnetic moment of Fe, when compared with experimental observations.[7, 12, 30, 34] In LF, the Hubbard U correction is included to the transition metal Fe only. The addition of DFT+U does not affect the O *2p* and La *5d* states, but does substantially change the Fe *3d* states, increasing the band gap and correcting the electronic structure.[34] The band gap

increases when the predominately unoccupied Fe *3d* states at the CBM, moves to lower

energy values with the increasing values of Hubbard U.[34]

2.4.4 Electronic Structures of Defects in Orthorhombic LaFeO$_3$

The addition of defects with different valences produces many interesting changes

to the electronic structure of the material. These interesting properties due to the defects,

such as vacancies and substitutions, can be evaluated using DFT calculations.[30, 35, 36, 37]

Generally, the RBM is utilized to analyze these electronic structures, which depend on

the total charge of the system. According to the RBM, in the LF system, when doped

with Sr at the La sites, holes are created due to charge imbalance.[30] Whereas, the removal

of an oxygen atom from the LF lattice creates free electrons, due to the charge imbalance

caused by the oxygen vacancy.[30] Different defects create acceptor and donor states within

the electronic structure that produces many interesting electronic properties that can be

evaluated in great detail using DFT.

2.4.5 Defect Formation Energy in Orthorhombic LaFeO$_3$

The changes to the thermodynamic properties due to defects can be evaluated

using the DFT methodology. Generally, DFT determines the energy of formation (ΔE_f) of

the defect in a system to predict if the defect forms spontaneously or requires additional

energy. The free energy of formation (ΔG_f) of a defect is described as:

$$\Delta G_f = \Delta E_f - T\Delta S_f + P\Delta V_f \tag{15}$$

Where ΔE_f is the change in total energy, which includes chemical potentials, ΔS_f is

primarily the change in vibrational entropy and ΔV_f is the change in volume due to the

defect.[38] Assuming the changes to entropy and volume due to the defect can be

negligible, the ΔG_f equals to only ΔE_f, which is the change in total energy.[38] Therefore, ΔE_f is described as:

$$\Delta E_f = E_{tot}^{defect} - E_{tot}^{perfect} \tag{16}$$

Where E_{tot}^{defect} and $E_{tot}^{perfect}$ are the calculated total energies of the defect and perfect systems, respectively. But, this formalism is not complete when the composition of the system is changed due to the defect; the formalism must include the external chemical potentials changed by the defect.[36] The external potentials are used for the atoms involved in the defect, or for charged defects can include the external potential of electrons.[36]

The following formalism for DFE is primarily obtained from Sundell *et al.*[36] and written in terms for defects in the LF system. The defect formation energy of an oxygen vacancy in LF is described as:

$$\Delta E_{V_O}^f = E_{V_O}^{tot}[LaFeO_{3-y}] - E^{tot}[LaFeO_3] + \mu_O \tag{17}$$

Where $E_{V_O}^{tot}$ and E^{tot} are the calculated total energies of the defect (oxygen vacancy) and perfect systems and μ_O is the chemical potential of oxygen. The defect formation energy formalism of Ca substitution at La site is described as:

$$\Delta E_{Ca}^f = E_{Ca}^{tot}[La_{1-x}Ca_xFeO_3] - E^{tot}[LaFeO_3] + \mu_{La} - \mu_{Ca} \tag{18}$$

Where E_{Ca}^{tot} and E^{tot} are the calculated total energies of the defect (Ca substitution) and perfect systems, μ_{La} and μ_{Ca} are the chemical potentials of La and Ca, respectively.

Determining DFE requires the use of external chemical potentials, which can be determined using the total energies of the corresponding bulk oxide. For example, the chemical potential of oxygen μ_O at zero Kelvin is described as:

$$\mu_O = \frac{1}{2}E^{tot}[O_2] \tag{19}$$

where $E^{tot}[O_2]$ is the total energy of an isolated oxygen dimer in a large supercell. The chemical potentials of La and Fe, have a range between rich and poor limits. Determining the La-rich limit depends on the total energies of the La_2O_3 oxide and oxygen molecule. The La-rich chemical potential μ_{La} is described as:

$$\mu_{La} = \mu_{La}^{La_2O_3} = \frac{1}{2}E^{tot}[La_2O_3] - \frac{3}{2}\mu_O \tag{20}$$

At the La-rich limit, the chemical potential μ_{La} is equilibrium with the bulk oxide La_2O_3, which leads La to precipitate for the LF lattice. So the chemical potential of La must be less than $\mu_{La}^{La_2O_3}$ to maintain the stability of the LF structure.

$$\mu_{La} < \mu_{La}^{La_2O_3} \tag{21}$$

Similarly, the Fe-rich limit depends on the total energies of the Fe_2O_3 oxide and oxygen molecule. The Fe-rich chemical potential μ_{Fe} is described as:

$$\mu_{Fe} = \mu_{La}^{Fe_2O_3} = \frac{1}{2}E^{tot}[Fe_2O_3] - \frac{3}{2}\mu_O \tag{22}$$

At the Fe-rich limit, the chemical potential μ_{Fe} is equilibrium with the bulk oxide Fe_2O_3, which leads Fe to precipitate for the LF lattice. So the chemical potential of Fe must be less than $\mu_{La}^{Fe_2O_3}$ to maintain the stability of the LF structure.

$$\mu_{Fe} < \mu_{Fe}^{Fe_2O_3} \tag{23}$$

The lower limits of the chemical potential for La and Fe can be determined utilizing the heat of formation of LF ($\Delta E^f_{LaFeO_3}$), described as:

$$\Delta E^f_{LaFeO_3} = E^{tot}[LaFeO_3] - \frac{1}{2}E^{tot}[La_2O_3] - \frac{1}{2}E^{tot}[Fe_2O_3] \qquad (24)$$

Where E^{tot} are the calculated total energies of the bulk LF, La_2O_3 and Fe_2O_3 structures, respectively.

The resulting chemical potential range of La can be described as:

$$\mu_{La}^{La_2O_3} + \Delta E^f_{LaFeO_3} < \mu_{La} < \mu_{La}^{La_2O_3} \qquad (25)$$

For a given potential energy of La (μ_{La}), the resulting chemical potential of Fe (μ_{Fe}) is described as:

$$\mu_{Fe} = \mu_{Fe}^{Fe_2O_3} + \Delta E^f_{LaFeO_3} + \mu_{La}^{La_2O_3} - \mu_{La} \qquad (26)$$

Therefore, in the La-rich condition, the chemical potentials for μ_{La} and μ_{Fe} are described as:

$$\mu_{La} = \mu_{La}^{La_2O_3} \qquad \text{and} \qquad \mu_{Fe} = \mu_{Fe}^{Fe_2O_3} + \Delta E^f_{LaFeO_3} \qquad (27)$$

Whereas in the Fe-rich condition, the chemical potentials for μ_{La} and μ_{Fe} are:

$$\mu_{La} = \mu_{La}^{La_2O_3} + \Delta E^f_{LaFeO_3} \qquad \text{and} \qquad \mu_{Fe} = \mu_{Fe}^{Fe_2O_3} \qquad (28)$$

The other chemical potential of interest is μ_{Ca} and is determined by a similar formalism utilizing the total energy of the bulk oxide CaO.

$$\mu_{CaO} = \mu_{Ca}^{CaO} = E^{tot}[CaO] - \mu_O \qquad (29)$$

Table 7.   The experimental and calculated lattice parameters of La$_2$O$_3$, Fe$_2$O$_3$, and CaO.

	Lattice parameters	Experimental	DFT
La$_2$O$_3$	a (Å)	3.940[16]	3.937[15]
	c (Å)	6.130[16]	6.129[15]
Fe$_2$O$_3$	a (Å)	5.427[21]	5.466[20]
	α (°)	55.280[21]	54.707[20]
CaO	a (Å)	4.81[24]	4.819[25]

As Table 7 shows the previously calculated lattice parameters of the bulk oxides La$_2$O$_3$, Fe$_2$O$_3$, and CaO are in good agreement with experimental observations.[15, 16, 20, 21, 24, 25]

3. COMPUTATIONAL METHODS

The first-principles based pseudopotential calculations were conducted based on DFT using the Quantum Espresso (QE) package.[39] All spin-polarized calculations used GGA, which uses the Perdew–Burke–Ernzerhof (PBE) exchange-correlation functional.[40] Vanderbilt ultra-soft pseudopotentials using nonlinear core corrections were used.[41] The pseudopotentials for La, Ca, and Fe were generated with scalar-relativistic calculations, whereas O was generated with non-relativistic calculation.[39] The valence states and electrons of the pseudopotentials are: La $5s^2$ $5p^6$ $5d^1$ $6s^{1.50}$ $6p^{0.5}$ has 11 electrons, Fe $3s^2$ $3p^6$ $3d^{6.5}$ $4s^1$ $4p^0$ has 16 electrons, O $2s^2$ $2p^4$ has 6 electrons, and Ca $3s^2$ $3p^6$ $4s^2$ $3d^0$ has 10 electrons. The structural optimizations were conducted using a single-point method, using the single consistent field (SCF) calculations. All the orthorhombic structures were further relaxed until the forces acting on the atoms were less than $1x10^{-3}$ Ry/a.u.[42]

The optimization of certain input parameters was an effort to find a compromise between lowering the computational stress, and achieving an acceptable accuracy in the calculated results. Generally, the input parameter is considered to be optimized when no significant energy gain is achieved with higher values of the input parameter.

3.1 Optimization of the Crystal and Magnetic Structures of Cubic $LaFeO_3$

A $2{\times}2{\times}2$ cubic supercell was utilized to find the optimized parameters, such as, lattice parameter, magnetic structures, E_{cut}, and K-points.
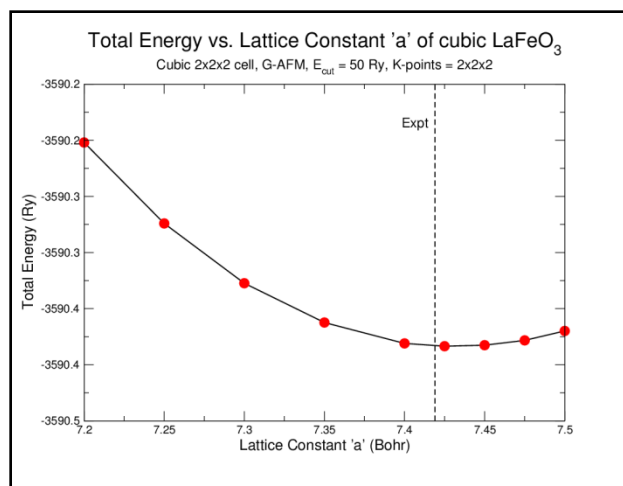
Figure 4. **The optimization of the lattice constant for cubic LaFeO$_3$, the dashed line indicates experimental lattice constant.[7]**

Figure 4 shows the optimization procedure to find the ground state energy structure by evaluating the total energy over a range of lattice constant 'a' values. Figure 3 shows the calculated lattice constant for cubic LF is 7.425 Bohr (3.929 Å), which is in good agreement with the experimental lattice constant 3.296 Å.[7] This overestimation of the lattice constant is a common feature expected while using the GGA methodology.[31]

Generally, GGA methodology increases the lattice constants by correcting the overbinding error present in the previous local density approximation (LDA) methodology, which generally underestimated the lattice constants.[26] But the GGA methodology overcorrects the overbinding error, which leads to the overestimation of the lattice constants.[26]
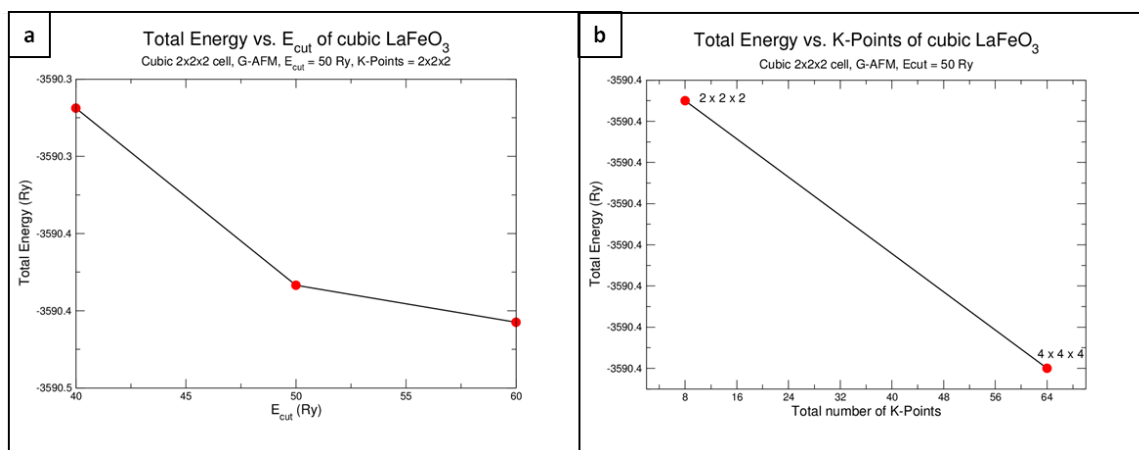
Figure 5. The optimization of (a) E_{cut} and (b) K-points for cubic LaFeO$_3$.

The optimization of E_{cut} was evaluated between 40, 50, and 60 Ry and the K-points considered were 2×2×2 and 4×4×4 points. As shown in Figure 5, the optimized E_{cut} and total number of K-points were 50 Ry and 2×2×2 points, respectively.

3.2 Optimization of the Crystal and Magnetic Structures of Orthorhombic LaFeO$_3$

The next goal was to obtain the optimized ground state orthorhombic LF configuration with the correct magnetic structure. The optimization of the orthorhombic LF was required to find the ground state configuration to ensure the validity of the model before the addition of defects such as Ca substitution at La sites and oxygen vacancies. The different optimized parameters included: lattice constant 'a', magnetic states, E_{cut} and K-points.
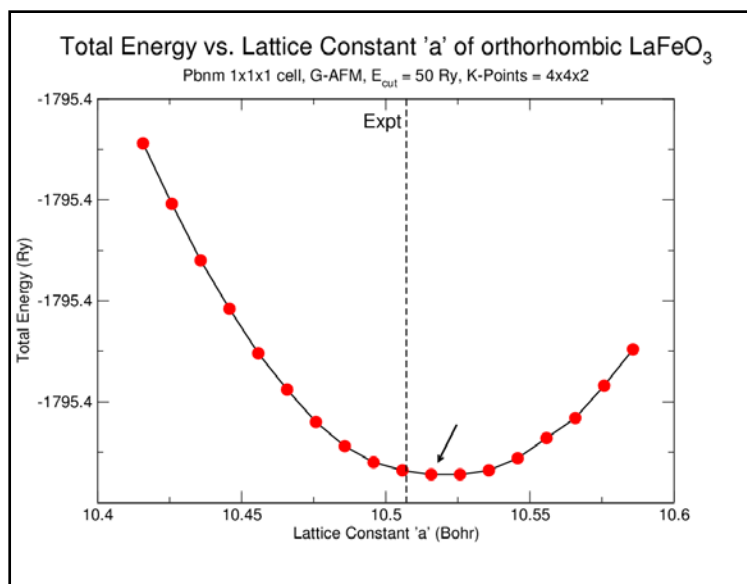
Figure 6. The optimization of the lattice constant 'a' for orthorhombic LaFeO$_3$, the dashed line indicates experimental lattice constant.[5] The arrow indicates the optimized ground state structure.

Utilizing the lattice constants gathered from experimental observations by Patrick Price and David Thomsen and incorporating the atomic positions from Dann *et al.*[10], the initial LF configuration was built. To optimize the crystal structure, the lattice constant 'a' was optimized, while lattice constants 'b and c' were set as ratios gathered from the experimental values. As Figure 6 indicates, the experimental lattice constant for 'a' is 10.5072 Bohr, while the calculated value is 10.5158 Bohr.[5] As discussed in Section 3.1, this overestimation of the lattice constant is a common feature expected while using the GGA methodology.[31]
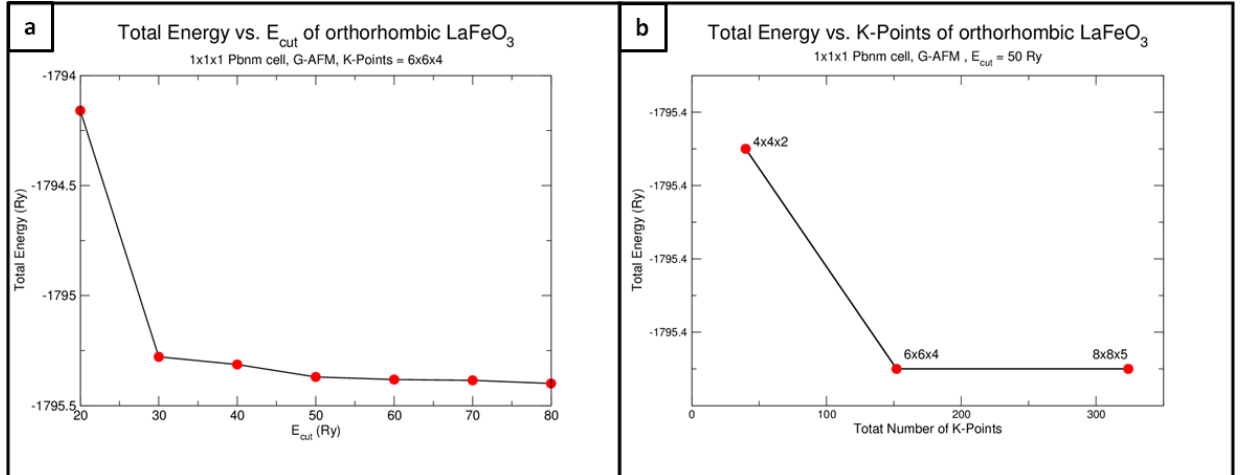
Figure 7. The optimization of (a) E_{cut} and (b) K-points for orthorhombic LaFeO$_3$

For optimizing the K-Points mesh, three different meshes of interest were $4\times4\times2$, $6\times6\times4$, and $8\times8\times5$, and the magnetic configuration and E_{cut} were set to G-AFM and 50 Ry respectively. For optimizing the E_{cut} energy, values between 20-80 Ry were of interest and the magnetic configuration and K-points mesh were set to G-AFM and $6\times6\times4$ respectively. Figure 7 shows the E_{cut} and K-Points optimization conducted for G-AFM LF, the optimized value of K-Points mesh used in $6\times6\times4$ mesh and E_{cut} of 60 Ry, where a larger mesh or higher E_{cut} energy will not significantly lower the ground-state energy.

Table 8. Calculated optimized input parameters for orthorhombic LaFeO$_3$ is compared with values obtained by Kizaki & Kusakabe.[29]

	Space Group	K-points	E_{cut} (Ry)	E_{den} (Ry)	Force (Ry/a.u)
This study	Pbnm	$6\times6\times4$	60	600	1×10^{-3}
Kizaki & Kusakabe.[29]	Pbnm	$3\times3\times2$	40	400	1×10^{-4}

As shown in Table 8, the optimized calculation parameters compare well with Kizaki & Kusakabe.[29] The further optimization of the atomic positions upon relaxation could provide a more accurate description of the model, which can be observed in the accuracy of the band gap and magnetic moments to experimental values.

3.3 Optimization of Hubbard U for LaFeO$_3$

The previously optimized orthorhombic LF structure was used to evaluate the effects of Hubbard U on the electronic structure. The Hubbard U value was only added to the Fe atoms, because Fe is a *3d*-transition metal that requires such an artificial correction. The first task was to find the magnetic ground-state structure, the four magnetic configurations of interest was A-AFM, C-AFM, G-AFM, and FM, respectively. Initially for values of U = 2, 4, and 6 eV, the lattice constant 'a' for these magnetic states were optimized using SCF calculations, as shown previously. The optimized ground state structure was G-AFM. Additionally, for the G-AFM configuration, the LF structure was further optimized for Hubbard U values of U = 1, 3, 5, 8, and 10 eV.

3.4 Optimization of the Supercells with Defects in LaFeO$_3$

The previously optimized orthorhombic LF structure was used to evaluate the effects of defects such as Ca substitution and O vacancy on the electronic structure. The E$_{cut}$ was set to 60 Ry in all cases. For the 2×1×1 and 2×2×1 supercells, the K-Points were 3×6×4 and 3×3×4, respectively.

3.5 Optimization for the Defect Formation Energy in LaFeO$_3$

The crystal structures of three bulk oxides (Fe$_2$O$_3$, La$_2$O$_3$, and CaO) were optimized by first setting the E$_{cut}$ value to 60 Ry, which is the previously optimized value

obtained from the orthorhombic LF structure. In terms of crystal parameters, only the lattice parameter 'a' was optimized in all three bulk oxides. All the other relevant lattice parameters, especially for Fe_2O_3 and La_2O_3, were set to ratios obtained from experimental values. Once the optimized structure was obtained, the K-points were optimized in all three oxides and finally the ground state structures were relaxed.

4. RESULTS AND DISCUSSION

4.1 Cubic LaFeO$_3$
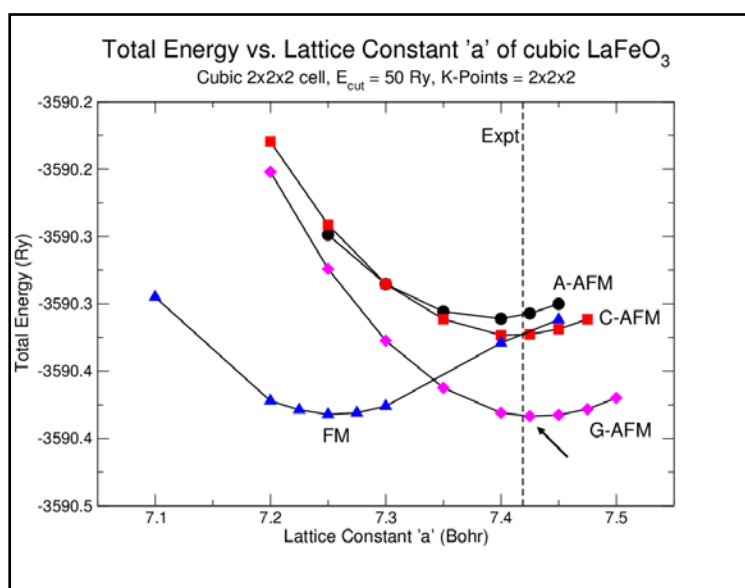
Figure 8. The total energy vs. lattice constant 'a' for four magnetic states (A-, C-, G-AFM, and FM) of cubic LaFeO$_3$. The dashed line indicates the experimental lattice constant.[7] The arrow indicates the ground state magnetic structure. The color image is available online.

For cubic LF, the four magnetic configurations evaluated were A-AFM, C-AFM, G-AFM, and FM, respectively. Figure 8 compares the ground state energies for the different magnetic states and indicates that the G-AFM state has the lowest energy and thereby is the most stable. The calculated ground state G-AFM lattice constant is 3.929 Å, which is slightly larger than the experimentally observed value of 3.926 Å.[7] In common, the GGA functional overestimates lattice constants, in comparison with experimental values.[31]

The total energy of the G-AFM structure is 0.0023 eV/LF lower than the FM structure; this energy difference is very small. To confirm that the G-AFM was the ground state magnetic state, both the G-AFM and FM structures were allowed to be fully relaxed. The relaxed G-AFM structure was still more energetically favorable when compared with the relaxed FM structure. The lattice constant of the fully relaxed G-AFM structure was 3.925 Å, which is closer to the experimental value of 3.926 Å, the previously unrelaxed calculated result of 3.929 Å.

Table 9.   Comparing the theoretical and experimental lattice constants of cubic LaFeO$_3$ for the G-AFM and FM magnetic structures.

	Method	G-AFM (Å)	FM (Å)
This Work	DFT	3.925	3.829
Lee *et al.*[27]	DFT	3.821	3.868
Lee *et al.*[27]	DFT+U	3.943	3.940
Koehler & Wollan.[7]	Experimental	3.926	N/A

Table 9 shows that the fully relaxed calculated lattice constant for G-AFM is in good agreement with the values found in literature.[7, 27] Lee *et al.*[27] underestimates the lattice constant and improves the lattice constant for G-AFM by introducing the correction term known as DFT+U. For the FM state (Table 9), the fully relaxed calculated lattice constant is 3.829 Å, which is in good agreement with Lee *et al.*[27], but both results are underestimated when compared with the experimental value.[7] Lee *et al.*[27] improves the lattice constant for the FM state by introducing the correction term known as DFT+U.
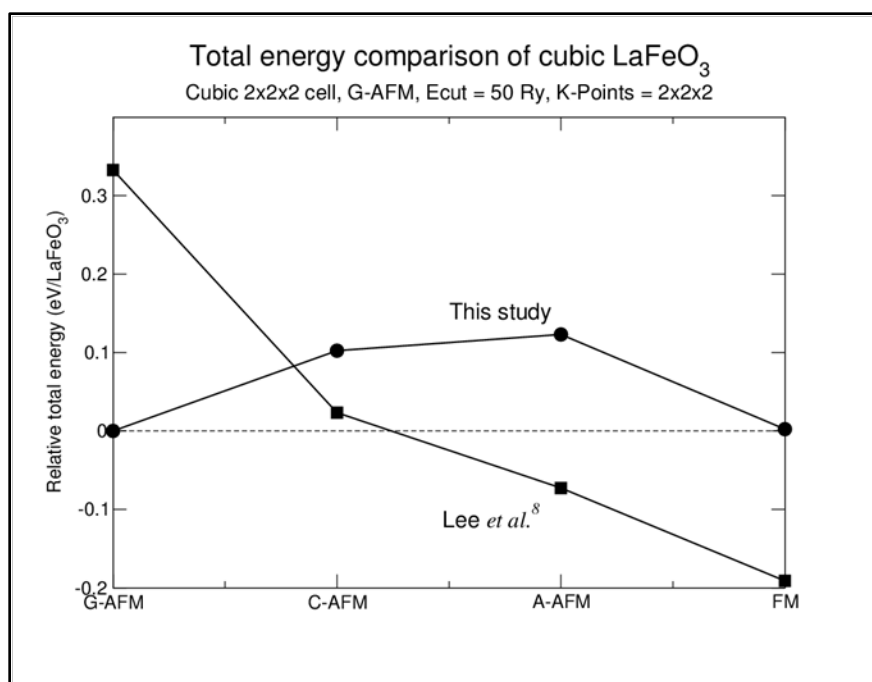
Figure 9. **Comparing the calculated relative total energy (eV/LaFeO₃) for the four different magnetic configurations between this study and those of Lee *et al.*[8]**

It is important to compare the results of the ground state energies for the different magnetic structures of cubic LF with previous literature.[8] As shown in Figure 9, the relative total energy (eV/LF) of all the calculated magnetic structures are plotted and compared with the results of Lee *et al.*[8] As previously discussed, the calculated ground state energies indicate that the G-AFM state is the ground state energy state and is therefore set to zero in Figure 9. On the other hand, results from Lee *et al.*[8] indicate that the G-AFM structure has the highest energy (least stable) and the FM structure has the lowest energy (most stable).

Generally, basic DFT methodologies are not equipped to study temperature-dependent material phases and the cubic phase is not the ground state configuration of bulk LF, but a high temperature phase. Therefore, no major conclusions can be gathered from the evaluation of the different magnetic structures for cubic LF in comparison with

available literature, because it is beyond the regime of generic DFT methodologies. But, this exercise of working with different magnetic structures will come in use when the ground state orthorhombic structure will be evaluated in greater detail, as discussed in Section 4.2.1.
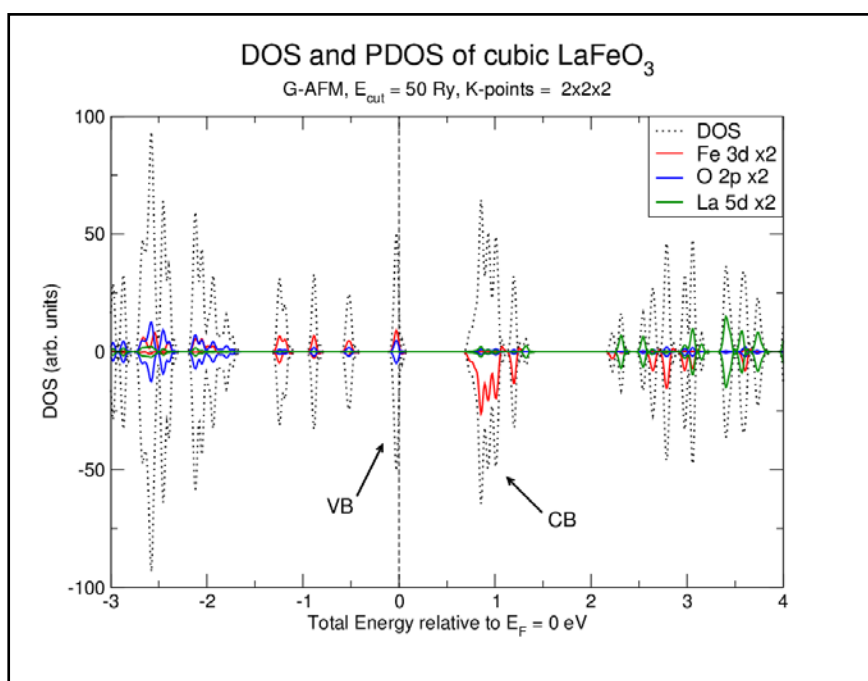
Figure 10. **The DOS and PDOS of cubic LaFeO$_3$. The individual orbitals are La 5d (green), Fe 3d (red), and O 2p (blue). The orbitals are magnified by two. The arrows indicate the valence and conduction bands. The color image is available online.**

Figure 10 shows the DOS and PDOS of cubic G-AFM LaFeO$_3$. The DOS in Figure 10 indicates that cubic LF is metallic in nature because there is no band gap at the E$_F$, which is in good agreement with previous calculated results.[27] Lee *et al.*[27] suggested that the bulk cubic LF structure has a high spin state and the delocalized electrons make the system metallic.

The nature of bonding in the cubic LF system can be better understood by analyzing the PDOS of the important valence orbitals, such as, Fe *3d*, La *5d*, and O *2p*

orbitals (Figure 10). Above the E_F, in the CB, the orbitals consists primarily of Fe *3d* states; this is in good agreement with Lee *et al.*[27] The delocalized nature of the Fe *3d* orbitals at the E_F makes the system metallic, confirming the results with Lee *et al.*[27] The states below the E_F in the VB consists primarily of both Fe *3d* and O *2p* states.

Below the E_F, from approximately 0 to -1.3 eV, the bands are dominated by the Fe *3d* orbitals with minor contributions from the O *2p* orbitals. The region between 0 to -1.3 eV indicates a small degree of hybridization between the Fe *3d* and O *2p* orbitals. But, approximately between the energy region 2 to 2.5 eV consists of equal amounts of Fe *3d* and O *2p* orbitals, which indicates a high level of covalent bonding between these orbitals. On the other hand, above the E_F, approximately between the energy 3 to 4.5 eV, the states are dominated by La *5d* orbital, which is an indication of the ionic bonding between the La and O.

Table 10.   Comparing the calculated and experimentally observed band gap and magnetic moment of Fe for cubic LaFeO$_3$.

	Method	Band gap (eV)	Fe magnetic moment (μ_B)
This study	DFT	0	3.75
Lee *et al.*[27]	DFT	0	3.5
Lee *et al.*[27]	DFT+U	2.0	3.9
Koehler & Wollan.[7] Arima *et al.*[12]	Experimental	2.1	4.6±0.2

As Table 10 indicates, the calculated band gap is in good agreement with a previous calculation of Lee *et al.*[27], indicating that cubic LF is metallic. Also, the calculated magnetic moment of Fe is in good agreement with Lee *et al.*[27] The apparent underestimation of the band gap and magnetic moment is an inherent error within the

generic formalisms of DFT. As shown by Lee *et al.*[27], the addition of Hubbard U or DFT+U can improve the magnetic moment and band gap of the system.

4.2 Orthorhombic LaFeO$_3$
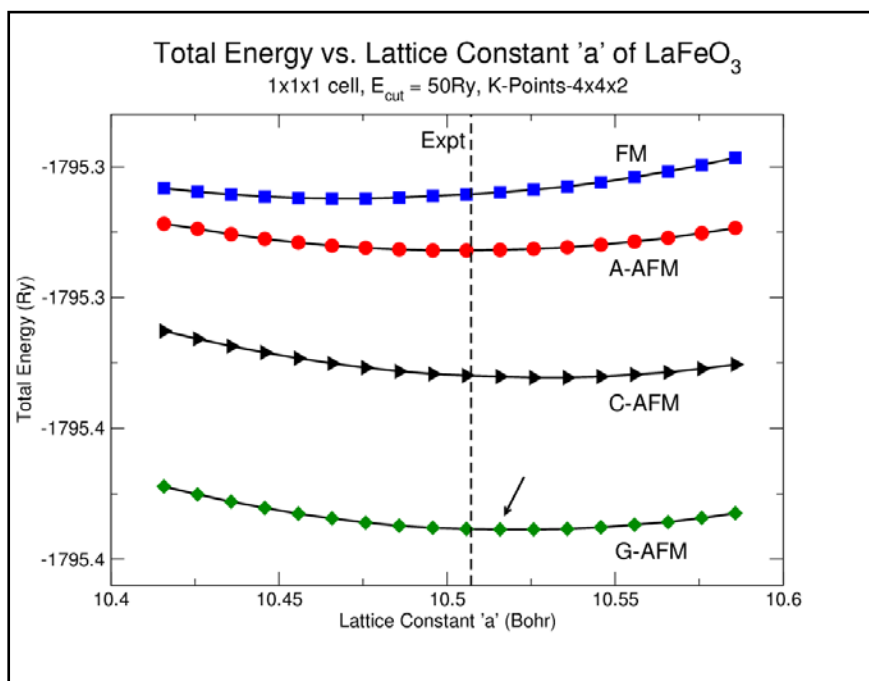
Figure 11. **Total energy vs. lattice constant for four magnetic states (A-, C-, G-AFM and FM) of orthorhombic LaFeO$_3$. The dashed line indicates the experimental lattice constant.[5] The arrow indicates the calculated ground state energy of orthorhombic LaFeO$_3$. The color image is available online.**

As shown in Figure 11, the optimization of the four magnetic structures indicated the G-AFM state is the most stable for the orthorhombic LF system. This observation is confirmed by previous computational and experimental investigations.[5, 29, 30]

Table 11. **Comparing the calculated and experimentally observed lattice constants of orthorhombic LaFeO$_3$.**

	a (Å)	b (Å)	c (Å)
This study	5.564	5.574	7.866
Kizaki & Kusakabe.[29]	5.553	5.5602	7.8550
Ritzmann et al.[30]	5.556	5.563	7.867
Beausoleil et al.[5]	5.5602	5.5679	7.8550

As shown in Table 11, our calculated lattice constants for the orthorhombic LF system, agree well with previous computational[29, 30] and our experimental[5] observations.
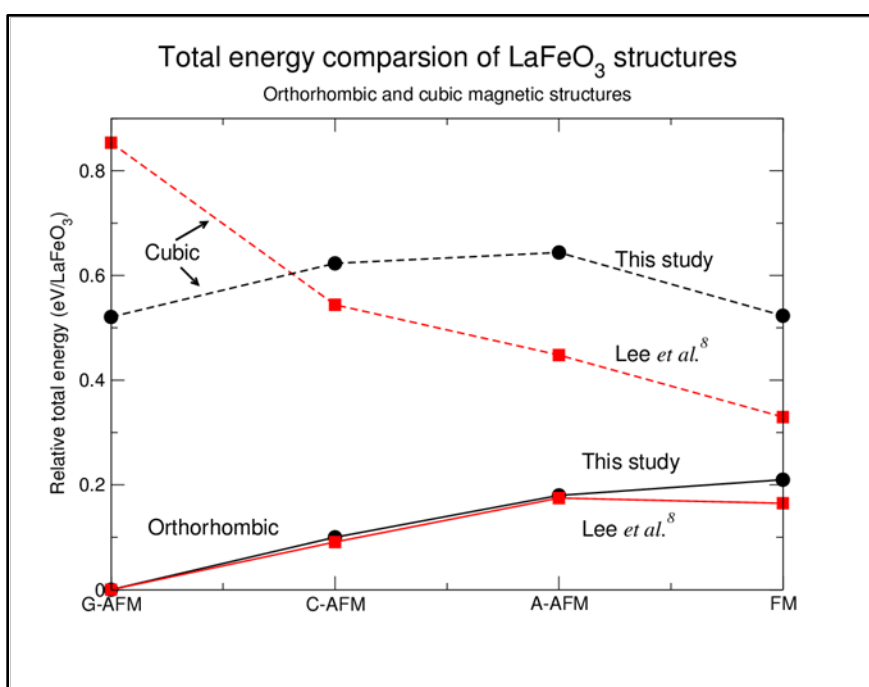
Figure 12. **Total energy comparisons of orthorhombic and cubic magnetic LF structures for our and Lee et al.[8] calculations. The color image is available online.**

As shown in Figure 12, the G-AFM orthorhombic configuration has the lowest ground-state energy when compared with various other magnetic configurations both

within the orthorhombic and cubic regime. The results of the relative total energy (eV/LF) for the various magnetic states in the orthorhombic cell is in good agreement with the calculated energy values determined by Lee *et al.*[8]

The electronic structure of the relaxed orthorhombic LF was calculated by determining the DOS and PDOS. The post processing of the PDOS of the electronic structure provides parameters such as band gap, magnetic moment per Fe atom, and an insight on chemical bonding, charge transfer, and spin states.
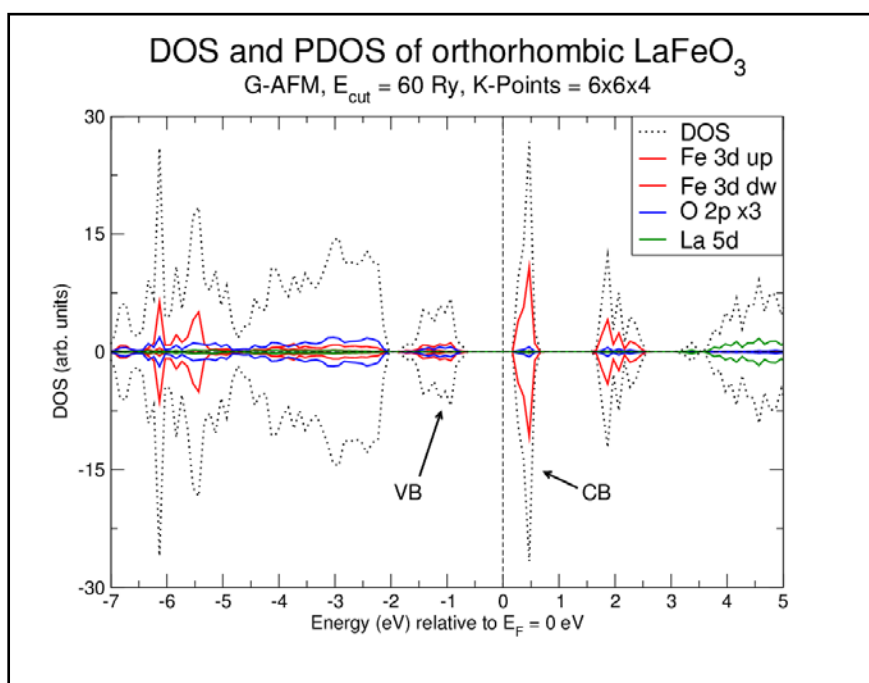
Figure 13. **The DOS and PDOS of orthorhombic LaFeO₃. The individual orbitals are La *5d* (green), Fe *3d* (red), and O *2p* (blue). Only the O *2p* orbital is magnified by three. The vertical dashed line at 0 eV indicates the Fermi energy. The arrows indicate the valence and conduction bands. The color image is available online.**

Figure 12 shows the electronic structures DOS and PDOS of the Fe *3d*, O *2p*, and La *5d* orbitals of the relaxed orthorhombic LF structure. Figure 13 shows there is a clear band gap between the VBM and CBM is approximately 0.81 eV, which is in good agreement with previous calculations.[8, 29, 30] This underestimation of the calculated band

gap of 0.81 eV when compared with the observed optical gap of 2.1eV[12] is an ubiquitous

failure present in the GGA functional.
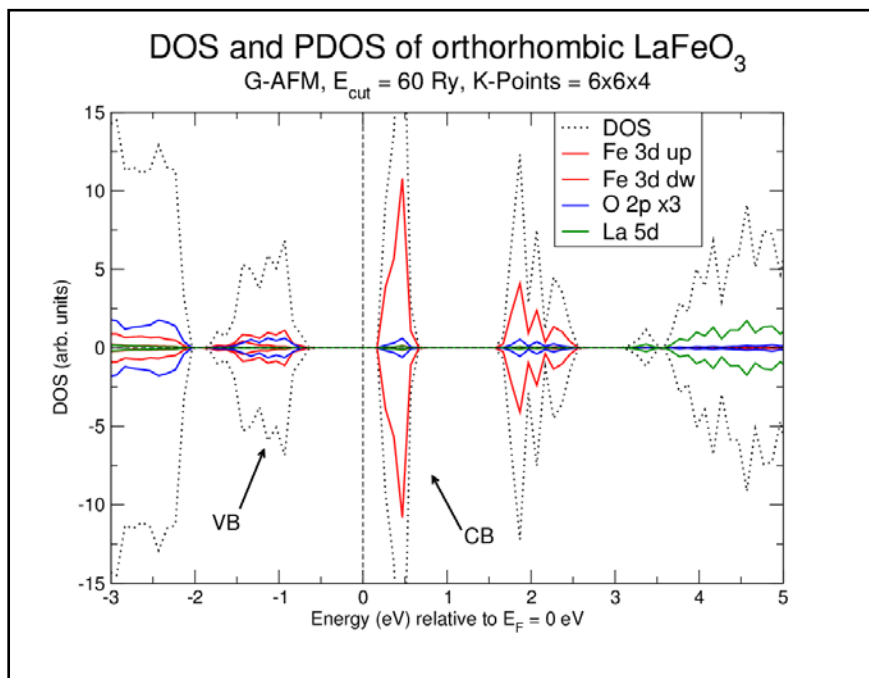
Figure 14. **The DOS and PDOS of orthorhombic LaFeO$_3$. The individual orbitals are La *5d* (green), Fe *3d* (red), and O *2p* (blue). Only the O *2p* orbital is magnified by three. The vertical dashed line at 0 eV indicates the Fermi energy. The arrows indicate the valence and conduction bands. The color image is available online.**

The electronic structure of orthorhombic LF matches well qualitatively and

quantitatively with previous experimental and theoretical findings.[12, 13, 29] The calculated

DOS for LF is in good agreement with experimental PES and XAS spectra[13] with respect

to states near the E$_F$. The calculated DOS and PDOS plots are nearly identical to a

previous calculated DOS and PDOS from orthorhombic LF conducted by Kizaki &

Kusakabe.[29] Therefore, the preliminary DOS for orthorhombic LF are comparable with

other experimental and theoretical finding, establishing the validity of the model. The

DOS peaks of the orthorhombic LF are roughly aligned with previous PES experimental

results, indicating the calculated structure has HS configuration for the Fe orbitals.[12, 13]

The evaluation of individual orbitals for La, Fe, and O, near the E_F, shows the important electronic characteristics of LF. Figure 13 shows the valence region can be considered between -0.5 to -2 eV, and comparing the valence peaks of the O *2p* and Fe *3d* orbitals, indicate a high degree of hybridization between these orbitals. The VB between -0.5 to -2 eV has approximately the same amount of Fe *3d* and O *2p* states, indicating a high degree of covalent bonding. The hybridization of Fe *3d* and O *2p* orbitals are expected in the FeO_6 octahedral and this is demonstrated in the states just below E_F.[12, 13, 29] In Figure 13, the PDOS region between -2 to -4 eV is dominated by O *2p* orbitals, and from -4 to -6 eV is dominated by Fe *3d* orbitals. Kizaki & Kusakabe.[29], reports roughly the same peak characteristics for the region between approximately -0.5 to -6 eV.

In Figure 14, the states above the E_F can also be broken down into three regions, first from 0.1 to 0.6 eV (CB), second from 1.5 to 2.5 eV, and third from 3.5 to 5 eV, respectively. In the first and second region, between 0.1 to 2.5 eV, the orbitals are dominated by unoccupied Fe *3d* states, which are confirmed by experimental observations.[13] The split between the first and second regions (0.1 to 2.5 eV) is due to the e_g-t_{2g} crystal-field splitting.[13] In the third region, between 3.5 to 5 eV, the states are dominated by unoccupied La *5d* states, which are confirmed by experimental observations.[13] The presence of unoccupied La *5d* states suggests the lack of covalent bonding between La-O and the bonding is more ionic in nature.

Table 12.   Comparing the calculated and experimentally observed band gap and magnetic moment of Fe for the orthorhombic LaFeO$_3$.

	Method	E$_g$ (eV)	μ_B per Fe atom
This study	DFT	0.81	3.7
Ritzmann et al.[30]	DFT	0.75	3.7
Kizaki & Kusakabe.[29]	DFT	0.89	4.1
Koehler & Wollan.[7] Arima et al.[12]	Experimental	2.1	4.6±0.2

As indicated in Table 12, the calculated band gap and magnetic moment of orthorhombic LF are underestimated compared to experimental observations.[7, 12] Previous calculated band gap and magnetic moments for orthorhombic LF are underestimated too due to the inherent errors present in the generic DFT (GGA) functionals.[29, 30] The underestimation can be corrected with the application of the Hubbard U model or better known as DFT+U.

4.3 The Effects of Hubbard U on Orthorhombic LaFeO$_3$

In this thesis, the linear-response approach was not implemented to find the appropriate Hubbard U value for LF. Therefore, all the discussion with respect to Hubbard U and its effect on the Fe *3d* orbitals are strictly qualitative.
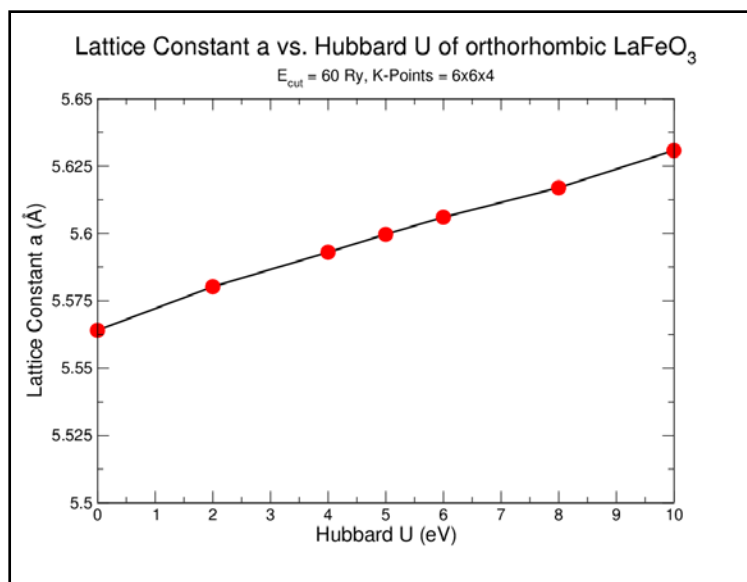
Figure 15.   Lattice Constant a vs. Hubbard U of orthorhombic LaFeO$_3$.

Figure 15 shows the optimized lattice constant 'a' increases almost linearly with increasing values of Hubbard U. This phenomenon was also observed by Ritzmann *et al.*[30], where the calculated lattice constant 'a' of LF with GGA+U (5.572 Å) was higher than the GGA value (5.556 Å).
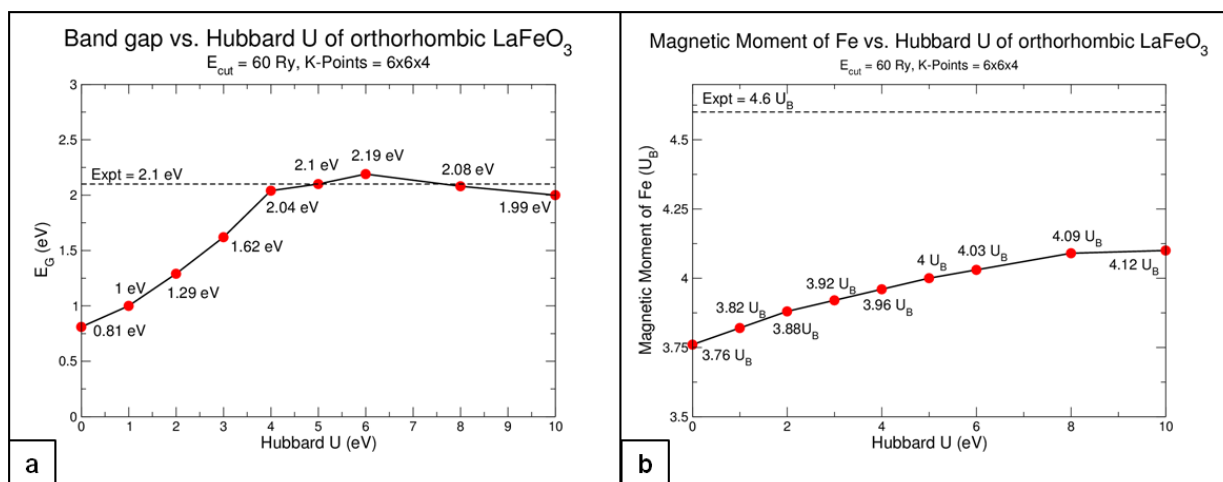
Figure 16.   a) The calculated band gap and b) magnetic moment of Fe vs. Hubbard U of orthorhombic LaFeO$_3$. The dashed lines indicate experimental band gap and magnetic moment of Fe.

Figure 16a shows the initially underestimated band gap for LF from a DFT calculation can be improved by the DFT+U methodology dramatically. Between value of U = 0-6 eV, the band gap increases as expected and at U = 5 eV the calculated band gap of 2.1 eV is in good agreement with the experimental optical band gap of 2.1 eV.[12] It is important to iterate that our calculations are not designed to find the optimized U value, but only to study the qualitative effects of U on the system. Figure 16b shows the magnetic moment of Fe increases almost linearly with increasing U between 0-10 eV, but the magnetic moments are still underestimated when compared with the experimental value.[7]

Figure 17. **a) DOS and b) PDOS vs. Hubbard U (U = 0, 4, 5 and 6 eV) of orthorhombic LaFeO₃. The dashed lines indicate the Fermi energy.**

Figure 17a shows significant changes occur to the electronic structure of orthorhombic LF, when the Hubbard U term is added. The band gap increases significantly as the value of U increases from 0 to 6 eV. As Figure 17a indicates the U value has no significant effects on the O $2p$ states in the VB. On the other hand, near the E_F, the states in the CB that are dominated by Fe $3d$ states move to energies above the E_F, which increase the band gap. As Figure 17b shows, the positions and shape of the Fe $3d$

states between -5 to -6 eV and the CB regions are affected by the Hubbard U term. Upon the addition of U, the Fe *3d* states in these two regions get narrower and are becoming localized states as observed by Yang *et al.*[34] too.

As the value of U increases, the Fe *3d* orbitals in the region between -5 to -6 eV moves to energy values below the E_F. For higher values of U, ultimately these Fe *3d* orbitals move away from the O *2p* orbitals and become localized.[34] According to Yang *et al.*[34], as the occupied Fe *3d* orbitals move to higher energies with the increase of U, these high spin electrons are hard to remove. Also, there are more occupied electrons in the spin up Fe *3d* states compared to the occupied spin down Fe *3d* states.[34] These two characteristics of the Fe *3d* states leads to the observed increase in the magnetic moment.[34] This might also explain the mechanism that increases the magnetic moment of Fe in the orthorhombic LF system (Figure 16b).

The change in the band gap as shown Figure 16a is connected to the position of the Fe *3d* states at the CB. Figure 17b shows the Fe *3d* states at the CB move above the E_F for U = 4, 5, and 6 eV, which increases the band gap. In Figure 16a for U = 0 eV, the Fe *3d* states has five valence electrons, and these electrons can be divided into two groups t_{2g}^3 and e_{2g}^2, respectively. For U = 0 eV, in the CB region, the Fe *3d* states closest to the E_F are dominated by t_{2g}^3 orbitals and the next Fe *3d* states lower in energy is dominated by e_{2g}^2 orbitals. The region dominated by t_{2g}^3 orbitals at the CB spontaneously move to lower energies upon the addition of U, thereby increasing the band gap. It is known that t_{2g}^3 orbitals are localized in nature and thus very sensitive and move spontaneously with increasing values of U.[34, 43]

On the other hand, the second Fe *3d* states region dominated by e_{2g}^2 orbitals do not move to lower energies as readily. The increasing U values have little effect on the region dominated by e_{2g}^2 orbitals; it moves slowly to higher energies, which decreases the splitting between the t_{2g}^3 - e_{2g}^2 orbitals. As shown in Figure 17b at U = 0 eV, this splitting was approximately 1 eV, but for U = 4 eV the splitting is very small, and further for values of U = 5 and 6 eV, there is no splitting at all.[34] It is known that e_{2g}^2 are less localized when compared to the t_{2g}^3 orbitals and therefore do not respond spontaneously to the Hubbard U values.[34, 43]

In Figure 16a, there are two different rates of increase for the band gap between U = 0 to 4 eV and U = 5 to 6 eV. The band gap increases linearly between 0 to 4 eV, and the rate of increase decreases for U = 5 to 6 eV, which is indicated by the different slopes present. The reason for the two slopes is evident in Figure 17b: the t_{2g}^3 - e_{2g}^2 orbitals have mixed, now the CB consists of e_{2g}^2 orbitals, which reduce the rate of increase in the band gap.[34]
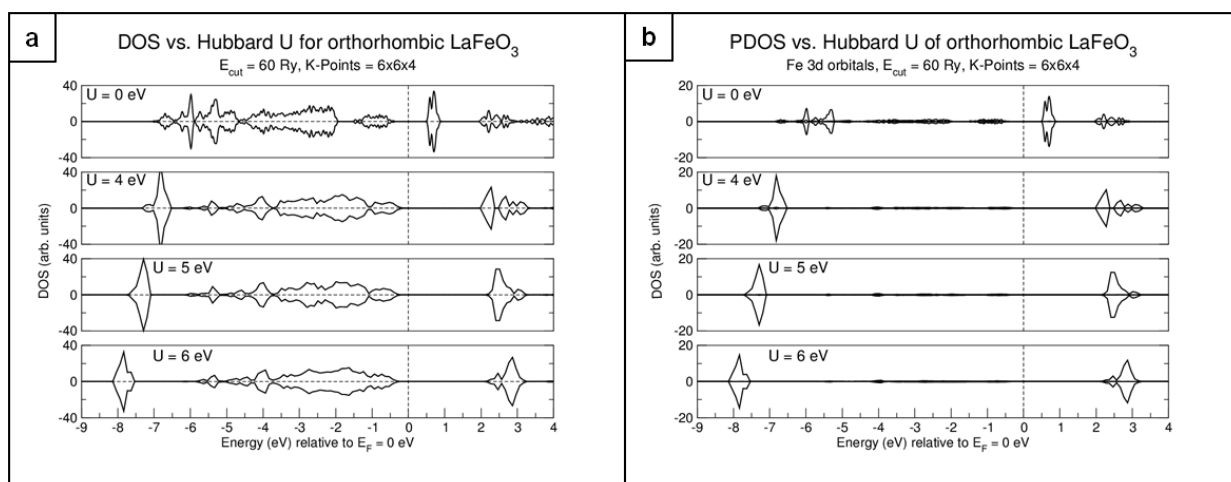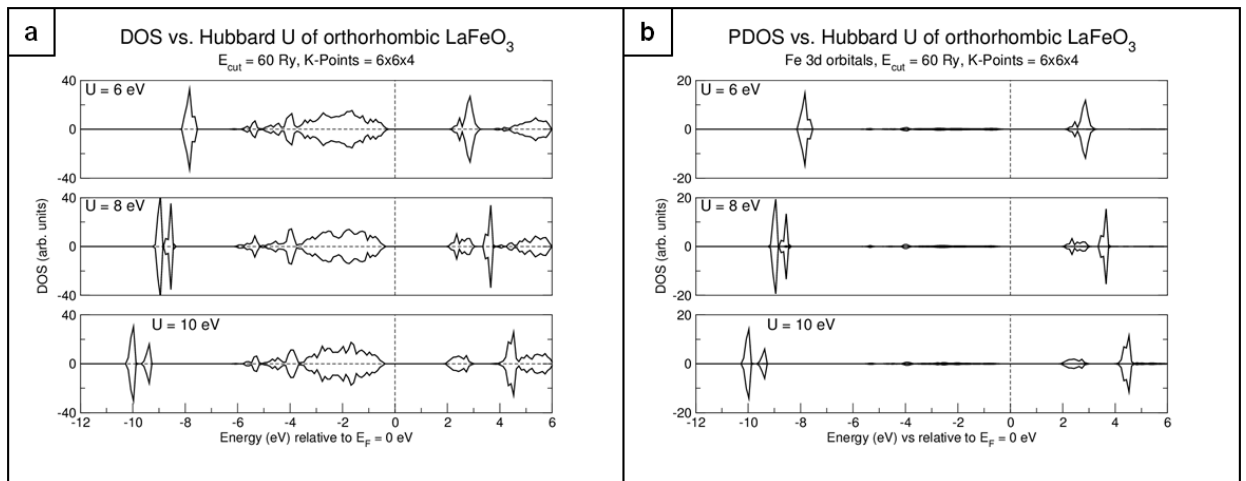

Figure 18.   **a) DOS and b) PDOS vs. Hubbard U (U = 6, 8, and 10 eV) of orthorhombic LaFeO₃. The dashed lines indicate the Fermi energy.**

Generally, for values greater than U = 5 eV, the LF orthorhombic system becomes unphysical, the appropriate U value most probably is between U = 4-5 eV. But Figure 18a shows the DOS for U = 6, 8, and 10 eV. The primary objective is to understand the effect of U on the Fe *3d* orbitals at the CB region. Figure 18a shows that the band gap of LF decreases for U = 8 and 10 eV. Figure 17b for U = 8 and 10 eV shows the t_{2g}^3 dominated orbitals keep on moving to higher energies, but e_{2g}^2 dominated orbitals start moving closer to the E_F, thereby decreasing the band gap.

In conclusion, the general survey of the effects of Hubbard U on the electronic structure of orthorhombic LF indicates that the addition of U significantly improves the electronic structure. Generally, the appropriate optimized U value from the linear-response approach would be probably between U = 4-5eV. The DOS and PDOS of Fe *3d* states for U = 4 and 5 eV show the band gaps are 2.04 and 2.1 eV, which is in good agreement with the observed optical gap is 2.1.[12] Also, the electronic structure for the LF system for U = 4 and 5 eV still maintains the essential characteristics of Fe-O covalent bonding in the VB and unoccupied Fe *3d* states in the CB, observed in previous theoretical and experimental works.[13, 30] Therefore, the DFT + U approach could be appropriate for the orthorhombic LF system.

4.4 The Electronic Properties of the Defects in Orthorhombic LaFeO₃

To investigate the electronic structures of the different defects in the orthorhombic LF system, two supercells 2×1×1 (40 atoms) and 2×2×1 (80 atoms) configurations were used. The 2×1×1 and 2×2×1 supercells may include some asymmetry features when a defect is included, because the lattice parameters are not expanded equally.[44] Therefore, the 2×2×2 supercell could be the best cell size to evaluate

the electronic structures of the defects, but with 160 atoms, this system is computationally very expensive.[44]

The electronic structures of both the 2×1×1 and 2×2×1 supercells for the different defects, with different charges, were investigated in great detail. The electronic structures were evaluated using the RBM to evaluate the effects of Ca substitution, oxygen vacancies, and the combination of these defects, in the perfect orthorhombic LaFeO$_3$ supercells.

4.4.1 Perfect LaFeO$_3$ Supercells
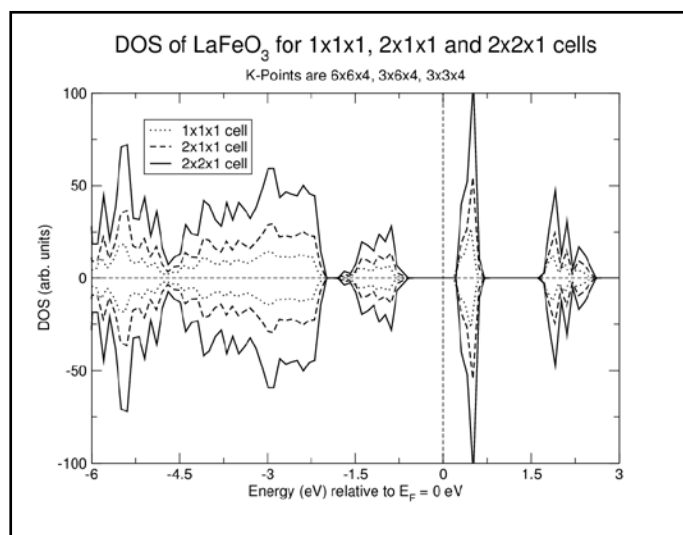
Figure 19.   **DOS of orthorhombic LaFeO$_3$ for 1×1×1, 2×1×1, and 2×2×1 cells, .**
The vertical dashed line at 0 eV indicates the Fermi energy.

As shown in Figure 19, the DOS of LaFeO$_3$ for the 1×1×1, 2×1×1, and 2×2×1 cells are qualitatively exact in nature, as was expected. All three cells indicate the LaFeO$_3$ system to be an insulator with a distinctive band gap of approximate 0.81 eV. The subsequent electronic structural changes due to the defects will be compared with the perfect electronic structure of the appropriate perfect 2×1×1 or 2×2×1 cells.

4.4.2 One Calcium Atom Substitution at La site (Ca$_{La}$)

The substitution of divalent point defects such as Ca (this study) or Sr (Ritzmann *et al.*[30]) at the La site in the orthorhombic LF system causes charge imbalance because La is trivalent. According to the RBM, to correct this charge imbalance, holes are introduced in the system to make the system neutral.[30]
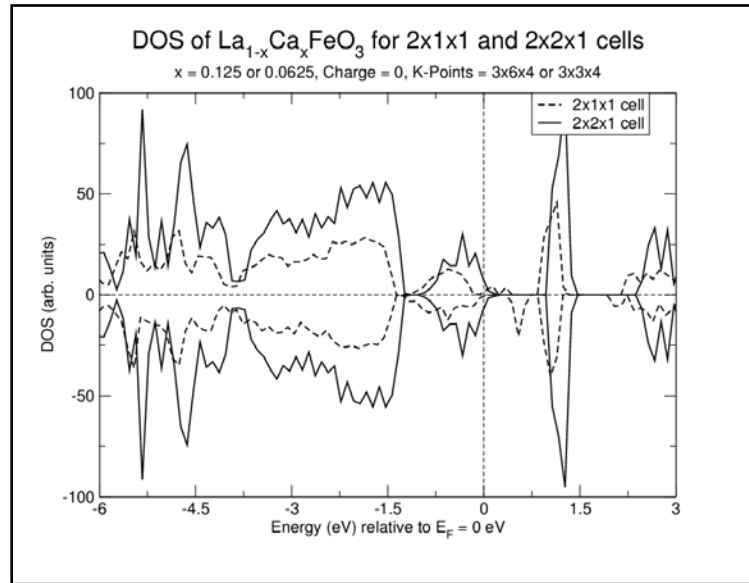
Figure 20. **The DOS of one Ca substitution at a La site (Ca$_{La}$) in orthorhombic LaFeO$_3$ for the 2×1×1 and 2×2×1 supercells. The total charge of the system is 0. The vertical dashed line at 0 eV indicates the Fermi energy.**

As Figure 20 indicates, significant changes occur to the electronic structure of LF, when it is doped with a single Ca atom in the 2×1×1 and 2×2×1 uncharged supercells. In both supercells, the addition of Ca creates holes in the lattice due to charge imbalance, which can be observed as the VBM moves above the E$_F$. Figure 20 show that the Ca point defect introduces unoccupied acceptor states above the E$_F$, which causes the system to no longer have a band gap, and exhibit p-type conductivity.

But there are major observable differences in the DOS for the two supercells, particularly between ~1 to -1 eV. In the 2×1×1 cell, the CB is asymmetric and the band is

an unphysical curve because the cell size is too small. On the other hand, the DOS for the larger 2×2×1 cell is very symmetric in nature and no unphysical curves are observed. Therefore, to obtain the accurate electronic structure for Ca doped LF, the larger 2×2×1 supercell is appropriate.
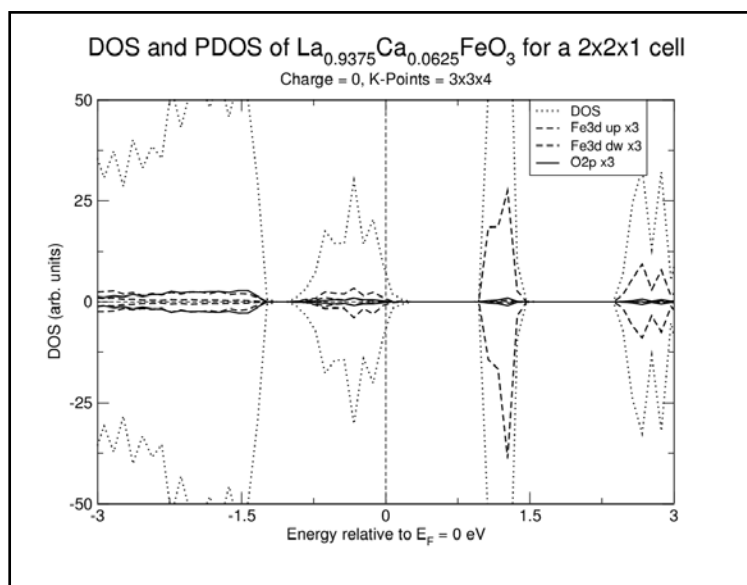
Figure 21.   **The DOS and PDOS of one Ca substitution at a La site (Ca$_{La}$) in orthorhombic LaFeO$_3$ for the 2×2×1 supercell. The individual orbitals are Fe *3d* and O *2p*. The orbitals are magnified by three. The total charge of the system is 0. The vertical dashed line at 0 eV is the Fermi energy.**

Figure 21 shows, the PDOS for the Ca doped LF provides greater insight on the nature of the holes introduced into the system. The PDOS (Figure 21) shows the holes include mixed Fe *3d* and O *2p* states, indicating the holes could be delocalized in nature. Ritzmann *et al.*[30] observed similar DOS and PDOS results for Sr doped LF and concluded the holes with mixed Fe *3d* and O *2p* states indicated the holes were "somewhat delocalized."
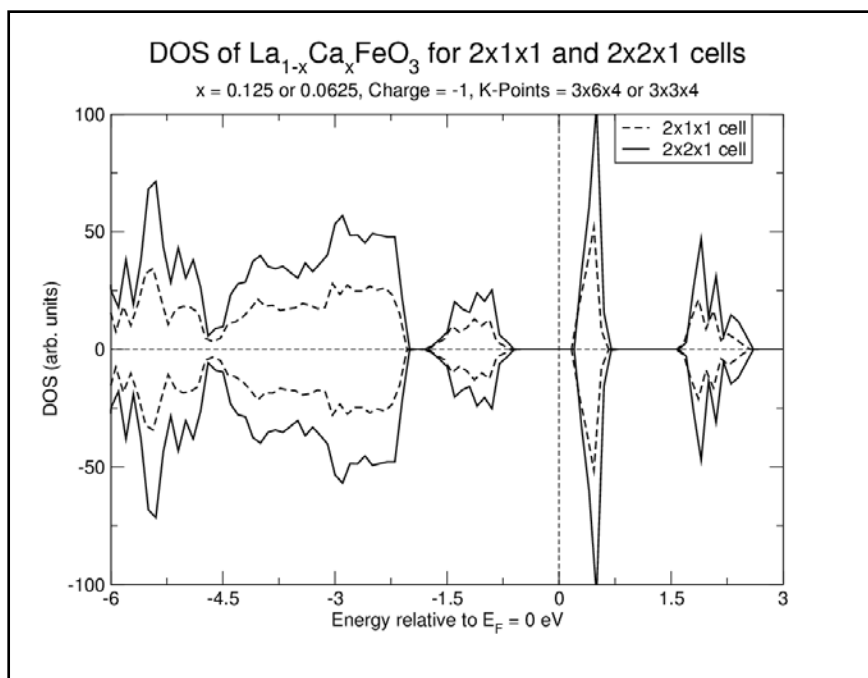
Figure 22. The DOS of one Ca substitution at a La site (Ca$_{La}$) in orthorhombic LaFeO$_3$ for the 2×1×1 and 2×2×1 supercells. The total charge of the system is -1. The vertical dashed line at 0 eV indicates the Fermi energy.

To evaluate the validity of the RBM predictions for the Ca doped LF system, a charge of -1 was introduced to remove the inherent charge imbalance due to the defect. Charging the system helps to determine the nature of the defects states that are present in the electronic structure. Figure 22 shows the electronic structures of Ca doped LF changes significantly when the system is charged. The introduction of a charge of –1 makes the entire system neutral, which can be observed with the absence of holes in the electronic structures for both supercells. The introduction of the charge re-introduces an approximate band gap of 0.77 eV.

In conclusion, the electronic structures for the uncharged Ca doped LF indicated the introduction of holes, and subsequent charging to remove the charge imbalance, indicated the absence of holes. This confirms that uncharged Ca doped LF exhibits p-type conductivity and is a semiconductor, which is agreement with literature.[30]

4.4.3 One Oxygen Vacancy (O_V)

The introduction of oxygen vacancies in the orthorhombic LF system causes charge imbalance in the form of extra electrons. The oxygen vacancies in a perovskite system, such as ABO_3, act as shallow donors.[36] Therefore, it is important to evaluate the effect of these extra electrons on the electronic structure of $LaFeO_{3-y}$ system, which has an oxygen vacancy.

Figure 23. The DOS of one oxygen vacancy (O_V) in orthorhombic $LaFeO_3$ for the $2\times2\times1$ and $2\times2\times1$ supercells. The total charge of the system is 0. The vertical dashed line at 0 eV is the Fermi energy.

Generally, the creation of an oxygen vacancy leaves behind two electrons that are absorbed by the *d* orbitals of the adjacent metal.[36] Similarly when an oxygen vacancy is created in the LF system, the two extra electrons are absorbed by two adjacent Fe atoms.[45] The Fe atoms that absorb the electrons reduce from Fe^{3+} to Fe^{2+} and are no longer in the HS regime.[45] As shown in Figure 23, the electronic structures change substantially with the creation of an oxygen vacancy. Unlike the electronic structures of

Ca doped LaFeO$_3$ (Figure 20), for the oxygen vacancy the electronic structures for both supercells are identical in nature.

As shown in Figure 23, the new defects states moves the CB below the E$_F$ and below the E$_F$ there are new occupied states due to the defect. Only some of the CB peaks are shifted below the E$_F$, while the rest of CB peaks are just above the E$_F$. When compared with the electronic structure of perfect LF, the creation of an oxygen vacancy introduces significant changes to the electronic structure. As Figure 23 shows, the DOS indicates the defect system has no band gap and exhibits n-type conductivity. The electronic structures in Figure 23, confirm that an oxygen vacancy acts as a shallow donor as previously observed.[36]
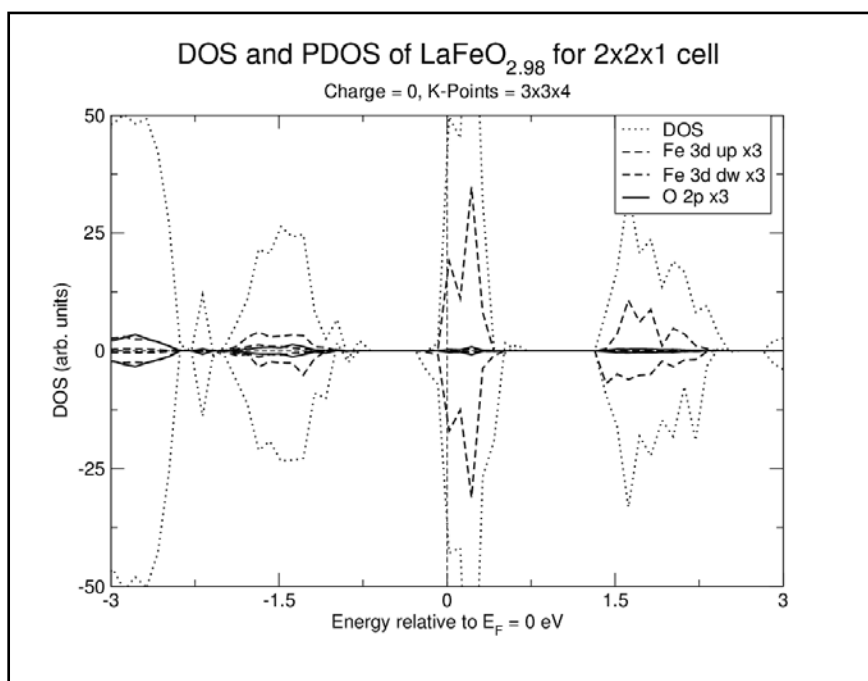
Figure 24. **The DOS and PDOS of one oxygen vacancy (O$_V$) in orthorhombic LaFeO$_3$ for the 2×2×1 supercell. The individual orbitals are Fe *3d* and O *2p*. The orbitals are magnified by three. The total charge of the system is 0. The vertical dashed line at 0 eV is the Fermi energy.**

Figure 24 shows the DOS and PDOS of an uncharged oxygen vacancy in a $2\times2\times1$ supercell. In Figure 24, the PDOS indicates that the occupied defect states just below the E_F are dominated by Fe $3d$ orbitals, in agreement with literature.[45] The PDOS indicates that the occupied defect states near the E_F are due to the two extra electrons left behind by the oxygen vacancy and are absorbed by nearby Fe $3d$ orbitals. The extra two electrons absorbed by the Fe $3d$ orbitals increase the Columbic repulsion, which shifts the CBM below the E_F, and makes the system an n-type semiconductor, in agreement with literature.[36]
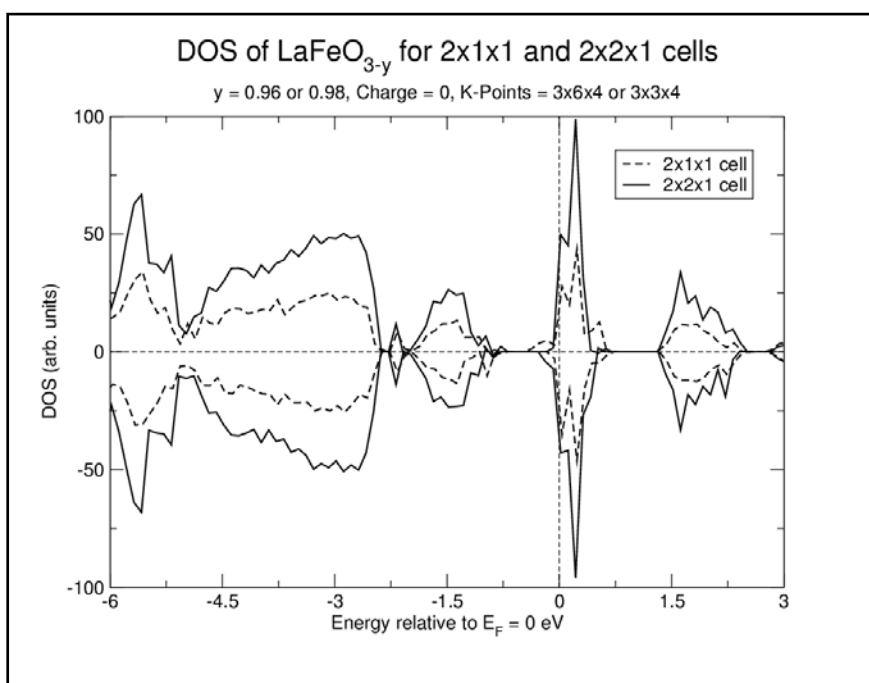

Figure 25. **The DOS of one oxygen vacancy (O_V) in orthorhombic LaFeO$_3$ for the $2\times2\times1$ and $2\times2\times1$ supercells. The total charge of the system is +1. The vertical dashed line at 0 eV is the Fermi energy.**

To investigate the validity of the RBM to describe the electronic structure of the oxygen vacancy, a charge of +1 was introduced into the system. The charge of +1 compensates only one of the two extra electrons and the system is still not neutral. Figure 25 shows the charged (+1) electronic structures of an oxygen vacancy in LF for both the

supercells. As shown in Figure 25, the charged electronic structures of the oxygen vacancy are more symmetric when compared with the uncharged counterparts in Figure 23.

As shown in Figure 25, there are no major observable differences between the electronic structures of both the supercells, suggesting that cell size has little difference on the electronic properties. The charge of +1 only partially compensates the negative charge due to the oxygen vacancy. The total charge of the system is still -1; the presence of the extra electron can be observed in the electronic structures in Figure 25. As expected from previous observations in Figure 24, the DOS of the charged oxygen vacancy for both supercells near the E_F exhibit n-type conductivity due to the extra electron. Further analysis of the PDOS for both supercells indicated the defects states just below the E_F were dominated by occupied Fe *3d* states, as expected from previous observations in Figure 24.

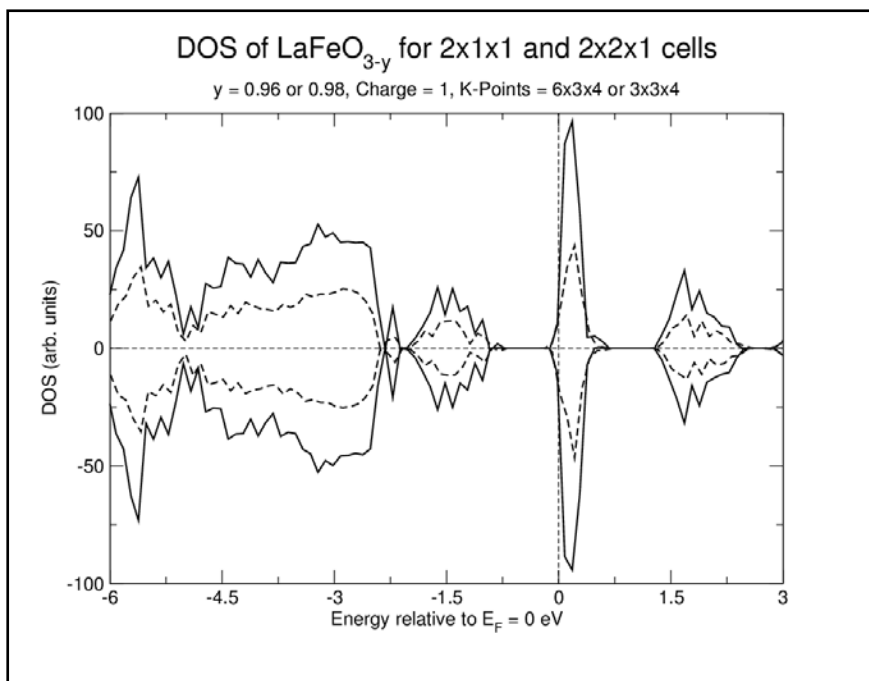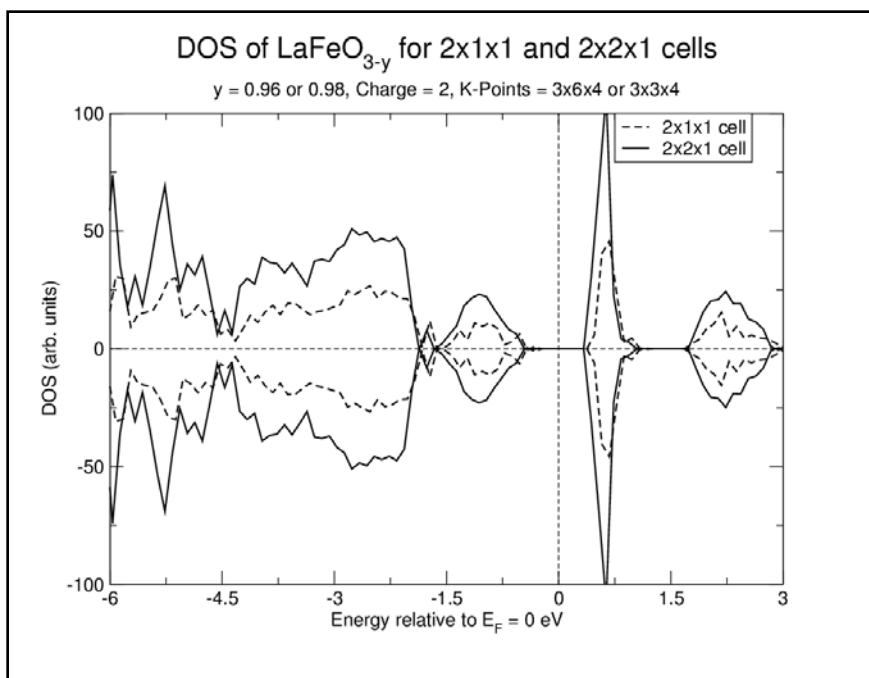**Figure 26.** The DOS of one oxygen vacancy (O_V) in orthorhombic $LaFeO_3$ for the $2\times2\times1$ and $2\times2\times1$ supercells. The total charge of the system is +2. The vertical dashed line at 0 eV is the Fermi energy.

To further investigate the RBM of this defect system, an artificial charge of 2 was introduced to completely compensate the presence of two extra electrons from the oxygen vacancy. Figure 26 shows the charged (+2) electronic structures of an oxygen vacancy in LF for both the supercells. As shown in Figure 26, there are no major observable differences between the electronic structures of both the supercells, suggesting that cell size has little difference on the electronic properties.

As shown in Figure 26, the electronic structures show the addition of the artificial charge (+2) compensates two extra electrons and the defect system returns to have insulator type characteristics. The electronic structures of the charged (+2) systems show the re-emergence of the band gap and states near the E_F agree well with the DOS of the perfect systems.

4.4.4 One Calcium Substitution and One Oxygen Vacancy ($Ca_{La} + O_V$)

The charge compensating mechanism for the holes introduced by the Ca doping is the creation of subsequent oxygen vacancies in the orthorhombic LF system.
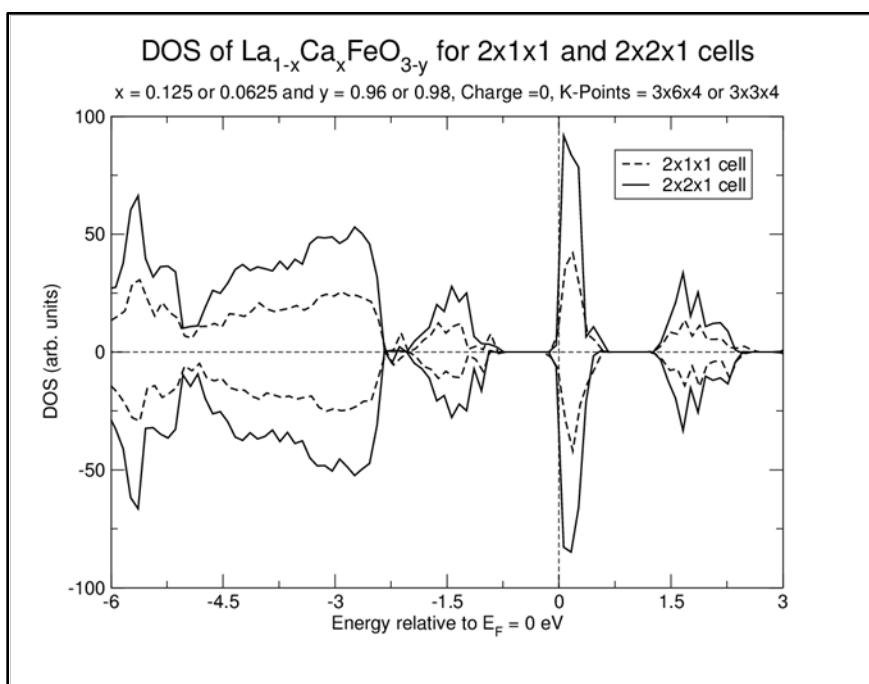
Figure 27.   **DOS of one Ca substitution and one oxygen vacancy ($Ca_{La} + O_V$) in orthorhombic LaFeO$_3$ for the 2×1×1 and 2×2×1 cells. The total charge of the system is 0. The vertical dashed line at 0 eV is the Fermi energy.**

Figure 27 shows the electronic structures of uncharged $La_{1-x}Ca_xFeO_{3-y}$ (one Ca substitution and one oxygen vacancy) for both the supercells. The DOS for both supercells are identical in nature, indicating there are almost no asymmetry contributions in both supercells. According to the RBM, a simple evaluation of the individual charges in this system, indicate the system has a -1 charge, and thereby must exhibit n-type conductivity. The combination of one Ca atom and oxygen vacancy leads to only partial charge compensation, the defect system still includes an extra electron, making the total charge to be -1. The extra electron within the lattice is observed in the DOS, as the

occupied states below the E_F, indicating n-type conductivity. The electronic structures in Figure 27 successfully confirms the predictions according to the RBM.
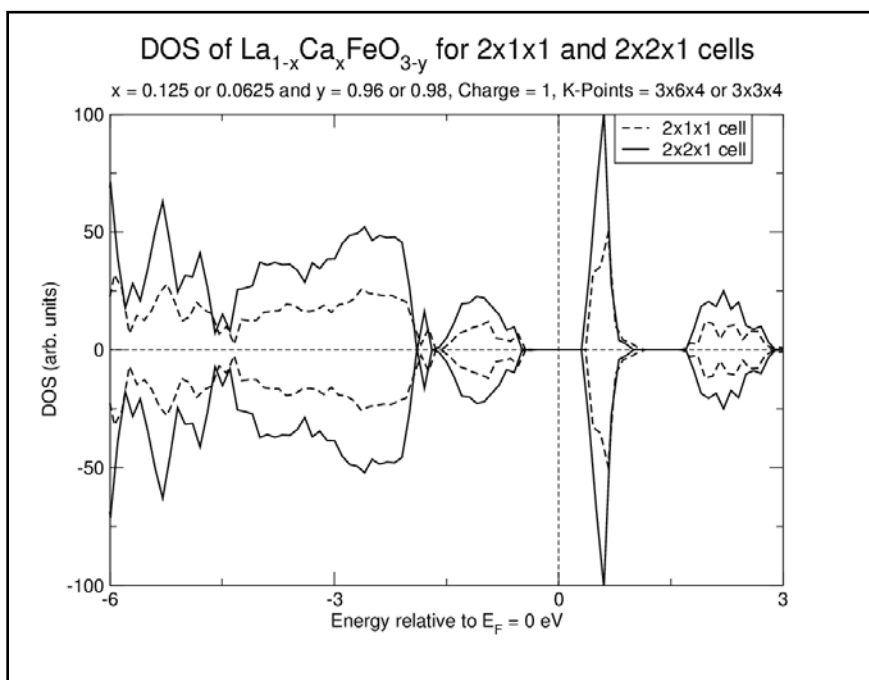
Figure 28. **DOS of one Ca substitution and one oxygen vacancy (Ca_{La} + O_V) in orthorhombic LaFeO$_3$ for the 2×1×1 and 2×2×1 cells. The total charge of the system is +1. The vertical dashed line at 0 eV is the Fermi energy.**

To further investigate the validity of the RBM, the defect system of $La_{1-x}Ca_xFeO_{3-y}$ was artificially charged to achieve neutrality. Figure 28 shows the DOS of the charged $La_{1-x}Ca_xFeO_{3-y}$ (one Ca substitution and one oxygen vacancy) for both the supercells. The DOS for both supercells are identical in nature, indicating there are almost no asymmetry contributions in both supercells. Figure 28 shows the addition of a charge +1 makes the system neutral, which can be observed in the electronic structures. The DOS indicates the defect system no longer exhibits the n-type conductivity, but there is a reemergence of a band gap of approximately 0.6 eV. In conclusion, the electronic structures for the uncharged $La_{1-x}Ca_xFeO_{3-y}$ (one Ca substitution and oxygen vacancy) indicated the presence of free electrons, and subsequent charging to achieve neutrality, indicated the

absence of free electrons. It is important to note the band gap of the charged defect system (~0.6 eV) is 0.21 eV lower than the perfect LF system (~0.81 eV), suggesting the introduction of the defects could enhance ionic-electronic conductivities within the system.

4.4.5 Two Calcium Substitutions and One Oxygen Vacancy ($2Ca_{La} + O_V$)
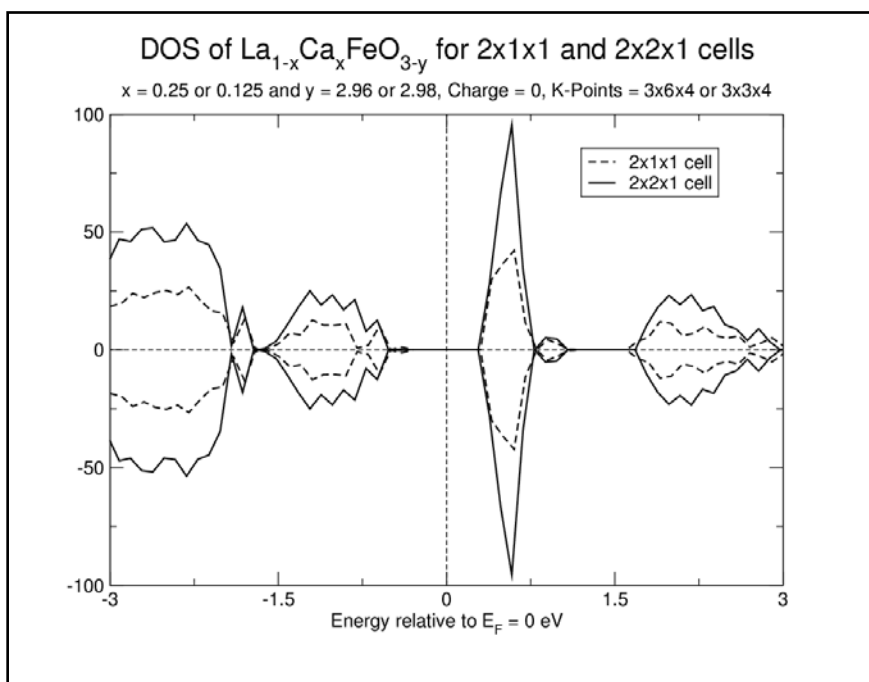
Figure 29. **DOS of two Ca substitutions and one oxygen vacancy ($2Ca_{La} + O_V$) in orthorhombic LaFeO₃ for the 2×1×1 and 2×2×1 cells. The total charge of the system is 0. The vertical dashed line at 0 eV is the Fermi energy.**

Figure 29 shows the electronic structures of uncharged $La_{1-x}Ca_xFeO_{3-y}$ (two Ca substitutions and one oxygen vacancy) for both the supercells. The DOS for both supercells are identical in nature, indicating there are almost no asymmetry contributions in both supercells. According to the RBM in a temperature-independent LF system, a simple evaluation of the individual charges in this system indicate the system is neutral, and thereby must exhibit a band gap (~0.58 eV). The combination of two Ca atoms and oxygen vacancy leads to complete charge compensation making the defect system

neutral. Figure 29 indicates the defect system no longer has any p-type or n-type conductivities due to charge compensations, but has a band gap of approximately 0.58 eV.

In conclusion, the electronic structures for the uncharged $La_{1-x}Ca_xFeO_{3-y}$ (two Ca substitutions and oxygen vacancy) systems indicated no defect (p-type or n-type) states near the E_F and have a distinctive band gap (~0.58 eV). The lowering of the band gap from 0.81 eV for the perfect LF to 0.58 eV for this defect system suggests the addition of these defects could promote ionic-electronic conductivities particularly at high temperatures.

4.5 Thermodynamic Properties of Defects in Orthorhombic LaFeO$_3$

To obtain the DFE of the three defect configurations in orthorhombic LF requires the use of chemical potentials. The chemical potentials μ_{La} μ_{Fe} μ_O and μ_{Ca} are obtained from the total energy obtained from the optimized structure.

Table 13. **Comparing the calculated lattice parameters of La$_2$O$_3$, Fe$_2$O$_3$ and CaO bulk oxides with previous theoretical and experimental observations.**

	Lattice parameters	Experimental	Theoretical	This Study
La$_2$O$_3$	a (Å)	3.940[16]	3.937[15]	3.905
	c (Å)	6.130[16]	6.129[15]	6.077
Fe$_2$O$_3$	a (Å)	5.427[21]	5.466[20]	5.440
	α (°)	55.280[21]	54.707[20]	55.280
CaO	a (Å)	4.81[24]	4.819[25]	4.836

As Table 13 shows the calculated lattice parameters of the bulk oxides La_2O_3, Fe_2O_3 and CaO are in good agreement with previous calculated and experimental observations.[15, 16, 20, 21, 24, 25] The calculated heat of formation ($\Delta E^f_{LaFeO_3}$) of LF for the 2×1×1 and 2×2×1 supercells are -0.3436 and -0.3439, respectively. The negative heat of formation indicates that orthorhombic LF is thermodynamically stable. The LF structure obtains lower ground state energy as a compound rather than existing as individual bulk oxides La_2O_3 and Fe_2O_3 respectively. Also, the calculated chemical potential of oxygen μ_O = -31.89 Ry. Utilizing the chemical potential of oxygen and the appropriate total energy of the relaxed bulk oxide structure, the chemical potentials of La, Fe, and Ca can be calculated using the previously described formalism in Section 2.4.5.

Table 14.   Comparing the calculated DFE results for the different defect configurations with Pushpa *et al.*[44] Pushpa *et al.*[44] used an E$_{cut}$ value of 50 Ry.

Defect Systems	This study				Pushpa *et al.*[44]	
	2×1×1 cell		2×2×1 cell		2×2×1 cell	
Charge = 0	DFE (eV)		DFE (eV)		DFE (eV)	
	La-rich	Fe-rich	La-rich	Fe-rich	La-rich	Fe-rich
Ca$_{La}$	-0.59	-0.94	-0.61	-0.95	-0.31	-0.65
O$_V$	4.89		4.83		4.21	
Ca$_{La}$ + O$_V$	3.17	2.83	3.13	2.78	2.60	2.26
2Ca$_{La}$ + O$_V$	1.43	0.74	1.49	0.79	1.15	0.47

As shown in Table 14, our calculated DFE (charge = 0) for the different defects systems are in good agreement with results of Pushpa *et al.*[44]

4.5.1 One Calcium Atom Substitution (Ca_{La})

As Table 14 indicates for the Ca doped LF system, the negative DFE for both the supercells suggest the defects can form spontaneously. The electronic structure (DOS) of the $2\times1\times1$ cell included some unphysical curves due to the asymmetry present, because the cell size was too small. Whereas, the electronic structure of the $2\times2\times1$ cell did not include any unphysical curves, because the cell size was large enough. But, the DFE results for both supercells for this defect are almost identical, suggesting the difference between the cell sizes did not have any effect on the thermodynamic properties.

The calculated DFE results for the Ca doped LF system for these supercells are in good agreement with Pushpa *et al.*[44] The DFE results indicate that the Ca defect more readily forms in a Ca environment, in a Fe-rich condition, rather than in a La-rich condition.[44]

4.5.2 One Oxygen Vacancy (O_V)

Table 15. **Comparing the calculate DFE of oxygen vacancy in the $2\times2\times1$ LaFeO$_3$ supercell, with previous theoretical and experimental observations.**

	Method	Symmetry	DFE (eV)
This study	DFT	Orthorhombic	4.83
Pushpa et al.[44]	DFT	Orthorhombic	4.21
Ritzmann et al.[30]	DFT+U	Pseudo-cubic	4.05
Pavone et al.[45]	DFT+U	Pseudo-cubic	~4.1
Lee et al.[27]	DFT+U	Pseudo-cubic	~4.4
Pavone et al.[45]	Experimental	Orthorhombic	~5.1

The calculated DFE for an oxygen vacancy in the $2\times1\times1$ and $2\times2\times1$ supercells are 4.89 and 4.83 eV, which is in good agreement with previous calculated and experimental observations (Table 15).[30, 44, 45, 46] The experimental oxygen vacancy formation energy in LF is high and it is approximately 5.1 eV.[45, 46] The experimental reaction enthalpy for the oxygen vacancy formation (~5.1 eV) was calculated by Pavone et al.[45] using the thermogravimetric data gathered from Mizusaki et al.[46]

The oxygen vacancy formation energy is high because of two processes with increase in the ground state energy of the LF system:[45]

1. An oxygen vacancy breaks the covalent bonds between a Fe-O-Fe.

2. The Fe^{3+} ions near the vacancy accept the two electrons from the vacancy and reduce to Fe^{2+}. These reduced Fe^{2+} ions are no longer in the more stable and energetically favorable high spin (HS) configuration.

The extra two electrons from the oxygen vacancy are absorbed by the two adjacent Fe atoms, creating new Columbic repulsion in the Fe^{2+} ions.[45] This increases the ground state energy and makes the oxygen vacancy formation energy to be high.[30] Table 14 shows the introduction of DFT+U can decrease the oxygen vacancy formation energy significantly when compared to the experimental observation by about 1 eV.[30, 45]

The calculated DFE for the oxygen vacancy (4.83 eV) could be high due to the breaking of the Fe-O-Fe covalent bonds and the reduction of Fe^{3+} ions to Fe^{2+} ions near the vacancy. The calculated electronic structure of the oxygen vacancy confirms the absorption of the two electron electrons from the oxygen vacancy into the LF sub-lattice. The PDOS indicates the extra electrons show up as new occupied states at the CBM and these states are predominately Fe *3d* states.

The high DFE of the oxygen vacancy suggests this defect is a temperature dependent defect. Therefore, at ambient conditions oxygen vacancy formation will be very improbable due to the high energy barrier, but with the addition of higher temperature, it would be easier to form and move oxygen vacancies.[44]

4.5.3 One Calcium Substitution and One Oxygen Vacancy (Ca_{La} + O_V)

As Table 14 indicates in the $La_{1-x}Fe_xO_{3-y}$ system, the addition of one Ca atom and oxygen vacancy is more energetically favorable, than only an oxygen vacancy. The DFE lowers significantly due to the partial charge compensation by to the annihilation of a

hole and extra electron. As expected, the DFE for the 2×2×1 supercell is little lower (more energetically favorable), than the 2×1×1 supercell. Our DFE results for both supercells are little higher, but in good agreement with the Pushpa *et al.*[44] The DFE results indicate that a defect system (one Ca atom and oxygen vacancy) more readily forms in a Ca environment, in a Fe-rich condition, rather than in a La-rich condition.[44]

4.5.4 Two Calcium Substitutions and One Oxygen Vacancy (2Ca$_{La}$ + O$_V$)

As Table 14 indicates in the La$_{1-x}$Ca$_x$FeO$_{3-y}$ system, the addition of two Ca atoms and oxygen vacancy is more energetically favorable than just one Ca atom and oxygen vacancy. The DFE lowers significantly due to the complete charge compensation by to the annihilation of the holes and extra electrons. Our DFE results for both supercells are little higher, but in good agreement with the Pushpa *et al.*[44] The DFE results indicate that a defect system (two Ca atoms and oxygen vacancy) more readily forms in a Ca environment, in a Fe-rich condition, rather than in a La-rich condition.[44] These results suggest the substitution of Ca atoms at La sites lowers the DFE of oxygen vacancies and increases its concentration significantly.[44] Therefore, as the concentration of oxygen vacancies increase, there are more available sites for the oxygen atoms to move around, leading to increased ionic conductivity.[44]

CONCLUSIONS

To summarize, the ground state crystal, magnetic, and electronic properties of LF and defect formation in LF was evaluated using DFT calculations. In cubic LF, due to the delocalized nature of the Fe $3d$ orbitals near the E_F, the cubic system is metallic in nature. Whereas, the electronic structures (DOS) indicated that orthorhombic LF is an HS insulator with a distinctive band gap. The PDOS provided a great insight into the hybridization present between occupied Fe $3d$ and O $2p$ orbitals in the VB and the unoccupied Fe $3d$ orbitals in the CB. Applying the DFT+U correction, the band gap of orthorhombic LF increased because the unoccupied Fe $3d$ orbitals in the CB moved to lower energies.

The electronic structures showed that the substitution of Ca at La sites introduced holes into the system, while the formation of an oxygen vacancy introduced extra electrons that are absorbed in Fe $3d$ orbitals. The subsequent charging of these systems to remove the charge imbalance showed that the resulting electronic structures were in agreement with the RBM. The combination of Ca substitutions and oxygen vacancy leads to charge compensation as expected. The thermodynamic model showed that calcium substitution at a La site was energetically favorable, while an oxygen vacancy formation was unfavorable. The high DFE for an oxygen vacancy indicated that adequate numbers of oxygen vacancies can only be achieved at high temperatures, and the subsequent combination of Ca atoms with oxygen vacancies reduced the DFE considerably.

REFERENCES

1. F. Bidrawn, S. Lee, J. M. Vohs, and R. J. Gorte, "The effect of Ca, Sr, and Ba doping on the ionic conductivity and cathode performance of LaFeO$_3$," *J Electrochem Soc,* 155[7] B660-B65 (2008).

2. M. H. Hung, M. V. M. Rao, and D. S. Tsai, "Microstructures and electrical properties of calcium substituted LaFeO$_3$ as SOFC cathode," *Mater Chem Phys,* 101[2-3] 297-302 (2007).

3. P. N. Dyer, M. F. Carolan, D. P. Butt, R. M. P. H. van Doorn, R. A. Cuter, and K. D. Gourley, "Mixed Conducting Membranes for Syngas Production"; Australian Patent No. #2001295502, 2005.

4. M. F. Carolan, P. N. Dyer, R. M. P. H. van Doorn, R. A. Cutler, and D. P. Butt, "Ion Transport Membranes for Syngas Production"; US Patent No. #6492290, 2003.

5. G. L. Beausoleil, P. Price, D. Thomsen, A. Punnoose, R. Ubic, S. Misture, and D. P. Butt, "Thermal Expansion of Alkaline-Doped Lanthanum Ferrite Near the Néel Temperature," *J Am Ceram Soc,* 97[1] 228-34 (2014).

6. M. C. Payne, M. P. Teter, D. C. Allan, T. A. Arias, and J. D. Joannopoulos, "Iterative Minimization Techniques for Abinitio Total-Energy Calculations - Molecular-Dynamics and Conjugate Gradients," *Rev Mod Phys,* 64[4] 1045-97 (1992).

7. W. C. Koehler and E. O. Wollan, "Neutron-Diffraction Study of the Magnetic Properties of Perovskite-Like Compounds LaBO$_3$," *J Phys Chem Solids,* 2[2] 100-06 (1957).

8. C. W. Lee, R. K. Behera, S. Okamoto, R. Devanathan, E. D. Wachsman, S. R. Phillpot, and S. B. Sinnott, "Stabilization Mechanisms of LaFeO3 (010) Surfaces Determined with First Principles Calculations," *J Am Ceram Soc,* 94[6] 1931-39 (2011).

9. H. Taguchi, Y. Masunaga, K. Hirota, and O. Yamaguchi, "Synthesis of perovskite-type (La$_{1-x}$Ca$_x$)FeO$_3$ ($0 \leq x \leq 0.2$) at low temperature," *Mater Res Bull,* 40[5] 773-80 (2005).

10. S. E. Dann, D. B. Currie, M. T. Weller, M. F. Thomas, and A. D. Alrawwas, "The Effect of Oxygen Stoichiometry on Phase-Relations and Structure in the System La$_{1-x}$Sr$_x$FeO$_{3-\delta}$ ($0 \leq x \leq 1$, $0 \leq \delta \leq 0.5$)," *J Solid State Chem,* 109[1] 134-44 (1994).

11. I. R. Shein, K. I. Shein, V. L. Kozhevnikov, and A. L. Ivanovskii, "Band structure and the magnetic and elastic properties of $SrFeO_3$ and $LaFeO_3$ perovskites," *Phys Solid State+,* 47[11] 2082-88 (2005).

12. T. Arima, Y. Tokura, and J. B. Torrance, "Variation of Optical Gaps in Perovskite-Type 3*d* Transition-Metal Oxides," *Phys Rev B,* 48[23] 17006-09 (1993).

13. H. Wadati, D. Kobayashi, H. Kumigashira, K. Okazaki, T. Mizokawa, A. Fujimori, K. Horiba, M. Oshima, N. Hamada, M. Lippmaa, M. Kawasaki, and H. Koinuma, "Hole-doping-induced changes in the electronic structure of $La_{1-x}Sr_xFeO_3$: Soft X-ray photoemission and absorption study of epitaxial thin films," *Phys Rev B,* 71[3] (2005).

14. K. J. Yoon, P. A. Zink, S. Gopalan, U. B. Pal, and L. R. Pederson, "Defect Chemistry and Electrical Properties of $(La_{0.8}Ca_{0.2})_{0.95}FeO_{3-\delta}$," *J Electrochem Soc,* 156[7] B795-B800 (2009).

15. N. Singh, S. M. Saini, T. Nautiyal, and S. Auluck, "Electronic structure and optical properties of rare earth sesquioxides (R_2O_3, R=La, Pr, and Nd)," *J Appl Phys,* 100[8] (2006).

16. W. C. Koehler and E. O. Wollan, "Neutron-Diffraction Study of the Structure of the A-Form of the Rare Earth Sesquioxides," *Acta Crystallogr,* 6[8-9] 741-42 (1953).

17. R. W. G. Wyckoff, "Crystal Structures,*"* pp. 7-8, Vol. 2, (1965).

18. G. Rollmann, A. Rohrbach, P. Entel, and J. Hafner, "First-principles calculation of the structure and magnetic phases of hematite," *Phys Rev B,* 69[16] (2004).

19. F. J. Morin, "Magnetic Susceptibility of αFe_2O_3 and αFe_2O_3 with Added Titanium," *Phys Rev,* 78[6] 819-20 (1950).

20. M. Blanchard, M. Lazzeri, F. Mauri, and E. Balan, "First-principles calculation of the infrared spectrum of hematite," *Am Mineral,* 93[7] 1019-27 (2008).

21. L. W. Finger and R. M. Hazen, "Crystal-Structure and Isothermal Compression of Fe_2O_3,Cr_2O_3, and V_2O_3 to 50 kbars," *J Appl Phys,* 51[10] 5362-67 (1980).

22. Y. Sato and S. i. Akimoto, "Hydrostatic compression of four corundum-type compounds: $\alpha-Al_2O_3$, V_2O_3, Cr_2O_3, and $\alpha-Fe_2O_3$," *J Appl Phys,* 50[8] 5285-91 (1979).

23. N. H. de Leeuw and J. A. Purton, "Density-functional theory calculations of the interaction of protons and water with low-coordinated surface sites of calcium oxide," *Phys Rev B,* 63[19] art. no.-195417 (2001).

24. P. Richet, H. K. Mao, and P. M. Bell, "Static Compression and Equation of State of CaO to 1.35 Mbar," *J Geophys Res-Solid,* 93[B12] 15279-88 (1988).

25. S. K. Medeiros, E. L. Albuquerque, F. F. Maia, J. S. de Sousa, E. W. S. Caetano, and V. N. Freire, "CaO first-principles electronic properties and MOS device simulation," *J Phys D Appl Phys,* 40[6] 1655-58 (2007).

26. J. G. Lee, "Computational Materials Science: An Introduction,*"* pp. 77-193, 1st ed. CRC Press, (2012).

27. Y. L. Lee, J. Kleis, J. Rossmeisl, and D. Morgan, "Ab initio energetics of LaBO_3(001) (*B*=Mn, Fe, Co, and Ni) for solid oxide fuel cell cathodes," *Phys Rev B,* 80[22] (2009).

28. W. L. Huang, Q. S. Zhu, W. Ge, and H. Z. Li, "Oxygen-vacancy formation in LaMO_3 (*M* = Ti, V, Cr, Mn, Fe, Co, Ni) calculated at both GGA and GGA + U levels," *Comp Mater Sci,* 50[5] 1800-05 (2011).

29. H. Kizaki and K. Kusakabe, "DFT-GGA study of NO adsorption on the LaO (001) surface of LaFeO$_3$," *Surf Sci,* 606[3-4] 337-43 (2012).

30. A. M. Ritzmann, A. B. Munoz-Garcia, M. Pavone, J. A. Keith, and E. A. Carter, "Ab Initio DFT+U Analysis of Oxygen Vacancy Formation and Migration in La$_{1-x}$Sr$_x$FeO$_{3-\delta}$ (x=0, 0.25, 0.50)," *Chem Mater,* 25[15] 3011-19 (2013).

31. C. Filippi, D. J. Singh, and C. J. Umrigar, "All-Electron Local-Density and Generalized-Gradient Calculations of the Structural-Properties of Semiconductors," *Phys Rev B,* 50[20] 14947-51 (1994).

32. M. Cococcioni and S. de Gironcoli, "Linear response approach to the calculation of the effective interaction parameters in the LDA+U method," *Phys Rev B,* 71[3] (2005).

33. H. J. Kulik, M. Cococcioni, D. A. Scherlis, and N. Marzari, "Density functional theory in transition-metal chemistry: A self-consistent Hubbard U approach," *Phys Rev Lett,* 97[10] (2006).

34. Z. Q. Yang, Z. Huang, L. Ye, and X. D. Xie, "Influence of parameters *U* and *J* in the LSDA+*U* method on electronic structure of the perovskites LaMO_3 (*M* = Cr,Mn,Fe,Co,Ni)," *Phys Rev B,* 60[23] 15674-82 (1999).

35. N. Shanthi and D. D. Sarma, "Electronic structure of electron doped SrTiO$_3$: SrTiO$_{3-\delta}$ and Sr$_{1-x}$La$_x$TiO$_3$," *Phys Rev B,* 57[4] 2153-58 (1998).

36. P. G. Sundell, M. E. Bjorketun, and G. Wahnstrom, "Thermodynamics of doping and vacancy formation in BaZrO$_3$ perovskite oxide from density functional calculations," *Phys Rev B,* 73[10] (2006).

37. W. Wei, Y. Dai, M. Guo, L. Yu, and B. B. Huang, "Density Functional Characterization of the Electronic Structure and Optical Properties of N-Doped,

La-Doped, and N/La-Co doped $SrTiO_3$," *J Phys Chem C,* 113[33] 15046-50 (2009).

38. A. F. Kohan, G. Ceder, D. Morgan, and C. G. Van de Walle, "First-principles study of native point defects in ZnO," *Phys Rev B,* 61[22] 15019-27 (2000).

39. P. Giannozzi, S. Baroni, N. Bonini, M. Calandra, R. Car, C. Cavazzoni, D. Ceresoli, G. L. Chiarotti, M. Cococcioni, I. Dabo, A. Dal Corso, S. de Gironcoli, S. Fabris, G. Fratesi, R. Gebauer, U. Gerstmann, C. Gougoussis, A. Kokalj, M. Lazzeri, L. Martin-Samos, N. Marzari, F. Mauri, R. Mazzarello, S. Paolini, A. Pasquarello, L. Paulatto, C. Sbraccia, S. Scandolo, G. Sclauzero, A. P. Seitsonen, A. Smogunov, P. Umari, and R. M. Wentzcovitch, "QUANTUM ESPRESSO: a modular and open-source software project for quantum simulations of materials," *J Phys-Condens Mat,* 21[39] (2009).

40. J. P. Perdew, K. Burke, and M. Ernzerhof, "Generalized gradient approximation made simple," *Phys Rev Lett,* 77[18] 3865-68 (1996).

41. D. Vanderbilt, "Soft self-consistent pseudopotentials in a generalized eigenvalue formalism," *Phys Rev B,* 41[11] 7892-95 (1990).

42. D. F. Shanno and K. H. Phua, "Algorithm 500: Minimization of Unconstrained Multivariate Functions [E4]," *ACM Trans. Math. Softw.,* 2[1] 87-94 (1976).

43. I. Solovyev, N. Hamada, and K. Terakura, "t_{2g} versus all $3d$ localization in LaMO$_3$ perovskites (M=Ti-Cu): First-principles study," *Phys Rev B,* 53[11] 7158-70 (1996).

44. R. Pushpa, D. Daniel, and D. P. Butt, "Electronic properties of Ca doped $LaFeO_3$: A first-principles study," *Solid State Ionics,* 249 184-90 (2013).

45. M. Pavone, A. M. Ritzmann, and E. A. Carter, "Quantum-mechanics-based design principles for solid oxide fuel cell cathode materials," *Energ Environ Sci,* 4[12] 4933-37 (2011).

46. J. Mizusaki, M. Yoshihiro, S. Yamauchi, and K. Fueki, "Nonstoichiometry and defect structure of the perovskite-type oxides $La_{1-x}Sr_xFeO_{3-\delta}$," *J Solid State Chem,* 58[2] 257-66 (1985).